A STUDY OF THE χ_1 CHARMONIUM STATE IN THE R704 EXPERIMENT AT CERN'S ISR

ARVE KYLLING

Thesis submitted to the degree cand. scient., University of Oslo.

"This day I saw with a pang of dismay, that

life is short and the hill – ranges long.

There was no time to be lost!"

W. H. Murray

"...What is good for the body is good for the whole man.

Our spirit is not separate from our body, any more than

than the water is separate from the stream.

The water is the stream."

Fred Rohe, The Zen of Running

Preface

In this work a description of the offline analysis of the χ_1 charmonium state in the R704 experiment performed at CERN's ISR is given. The χ_1 parameters m_{χ_1}, Γ, $\Gamma_{p\bar{p}}$ and $Br(\chi_1 \rightarrow p\bar{p})$ are also discussed. In appendix D preliminary results from the $^1P_1$ search is given.

I would like to thank my supervisor cand. real. Lars Bugge for his help and guidance. Also lots of thanks to cand. scient. Steinar Stapnes for many a claryfing discussion. I would also like to thank cand. scient. Bjarne Stugu for allowing me to use some of his results from the $^1P_1$ analysis. I am also grateful to dr. Arne Lundby for making my stays at CERN possible. Thanks to the Elementary Particle Physics group at the University of Oslo and the R704 collaboration. Finally I would like to thank my parents for their support.

Thanks to Chris, Leif, Maria, Morten and Steve.

Arve Kylling

CERN, 24.11.85

CONTENTS

TABLES

FIGURES

1. R704 AND CHARMONIUM

1.1 INTRODUCTION

Charmonium was discovered in November 1974 by two independent experimental groups: MIT−BNL led by Samuel Ting ($p\ Be \rightarrow e^+e^- +$ anything) [1] and SLAC−LBL led by Burton Richter ($e^+e^- \rightarrow$ hadrons) [2] both discovering the J/ψ state. Charmonium is a bound state of a charmed quark c and its antiquark $\bar{c}$. Charmed quarks were introduced theoretically in 1964 by Hara [3] and by Bjorken and Glashow [4] to construct a symmetrical model of four quarks (u, d, s, c) and four leptons (ν_e, e, ν_μ, μ). Later, in 1970, charmed quarks became even more necessary when it was shown by Glashow, Illiopoulos and Maiani that they can resolve some vital problems of weak interactions in kaon decay, the GIM−mechanism [5]. Also the ratio

$$R = \sigma(e^+ e^- \rightarrow \text{hadrons})/\sigma(e^+ e^- \rightarrow \mu^+ \mu^-) = \Sigma\, e_q^2$$

where the sum is over the charges of the different quark flavors , did not fit too well with data. The addition of a fourth quark with $e_q = 2/3$ (the charm quark) together with a coulor factor 3 would help upon this, see fig 1.

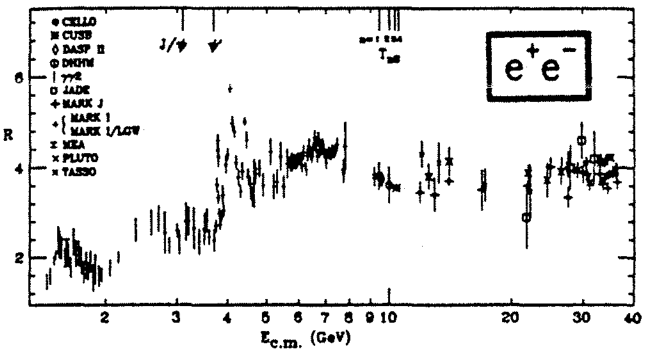

Figure 1: Measurements of $R=\sigma(e^+e^- \rightarrow \text{hadrons})/\sigma(e^+e^- \rightarrow \mu^+\mu^-)$ Observe the rise at charmonium energies. From [6].

After the "November-revolution" in 1974 charmonium has been extensively studied both experimentally and theoretically. Experimentally e^+e^- - collider machines have dominated the contribution to our knowledge about charmonium, but recently also a $p\bar{p}$ experiment (R704 at CERN's ISR) has given significant results. Theoretically charmonium can be described relatively simple. Being a heavy system it can be given a treatment based on the non-relativistic Schrodinger equation and a static potential. The strong interaction between the charmed quark and its antiquark is mediated by coulored gluons according to the theory of strong interactions, quantum chromo dynamics, (QCD). Charmonium spectroscopy is thus a good way of testing the basic ideas of QCD.

1.2 EXPERIMENTAL AND THEORETICAL FACTS ABOUT $c\bar{c}$

1.2.1 CHARMONIUM, A NON-RELATIVISTIC SYSTEM

The non-relativistic behaviour of charmonium can be illustrated through the application of the virial theorem:

$$2 < T > = < \vec{r} \cdot \vec{\nabla} V(r) >$$

where T is the kinetic energy of the system and V(r) is the potential between the c and the $\bar{c}$ quark separated by r . Conservation of energy implies:

$$< T > + < V > = E_b$$

where E_b is the binding energy. Introducing a confining potential $V(r) \sim r$ one gets:

$$2 < T > = < V(r) >$$

giving

$$3 < T > = E_b$$

or

$$m_q < v^2 > = E_b/3$$

where v^2 is the square of the q ($\bar{q}$) velocity and m_q the quark mass. For $c\bar{c}$ threshold is at the $3\ {}^3D_1$ state[1] and the binding energy is given by

[1] The spectroscopic notation is often used to denote the different charmonium states. We have

$$E_b = m(3\ ^3D_1) - m(1\ ^1S_0) = (3770 - 2980)\ \text{MeV} = 790\ \text{MeV}$$

The values for the masses are taken from [6]. Assuming $m_q \cong 1500$ MeV

$$< v^2 > = 790/4500 = 0.18$$

showing that the $c\bar{c}$ system can be given a non-relativistic treatment to a reasonable approximation [12].

1.2.2 THE SCHRODINGER EQUATION

The mass spectrum of charmonium can be calculated by applying the Schrodinger equation:

$$\{-1/m_q \nabla^2 + V(r)\}\ \psi_n(r) = E_n\ \psi_n(r)$$

where $\psi_n(r)$ is the system's wavefunction and E_n the eigenvalue (binding energy). A potential V(r) is needed, the exact form is not known, but several models have been suggested. They fall into two classes:

1. QCD-like models in which the asymptotic behaviour of the static $q\bar{q}$-potential in QCD is incorporated. Two such models are the Cornell model [7] and the Richardson model [2]. The Cornell potential

---

$$n\ ^{2S+1}L_J$$

where S is the total spin of the system, $\vec{S} = \vec{s}_1 + \vec{s}_2$, $\vec{s}_i$ spin quark i. $\vec{L}$ is the angular momentum, L = 0, 1, 2,... = S, P, D,... , and $\vec{J} = \vec{L} + \vec{S}$ is the total angular momentum, J = S for L = 0 and J = L−1, L, L+1 for L ≠ 0. n is the principal quantum number.

The charmonium states are also frequently denoted by their J^{PC} quantum numbers, $P = (-1)^{L+1}$ and $C = (-1)^{L+S}$, parity and charge conjugation respectively. E.g.

$$\chi_1 = 1\ ^3P_1 = 1^{++}$$, see also table 1.

The J^{PC} of the different states have been determined by studying the allowed decay channels of the different states (C and P conservation) and by doing an angular correlation of the cascade process

$$\psi' \to \gamma\ \chi_J \to \gamma\ \gamma\ J/\psi \to \gamma\ \gamma\ l^+\ l^-\ ,\quad l^\pm = \text{lepton}$$

For a discription of the method see [17]. For the ψ see [31] and for the χ_1 and χ_2 state see [18].

$$V(r) = -4/3\,\alpha_s/r + k\,r$$

consists of a static Coulomb field $V(r) \sim -4/3\,\alpha_s/r$ which gives the one gloun exchange at short distances (asymptotic freedom) and the term $V(r) \sim k\,r$, which gives a linear increase of the binding energy at large distances (confinement), see fig. 2 , α_s is the strong coupling, and k the tension strength.

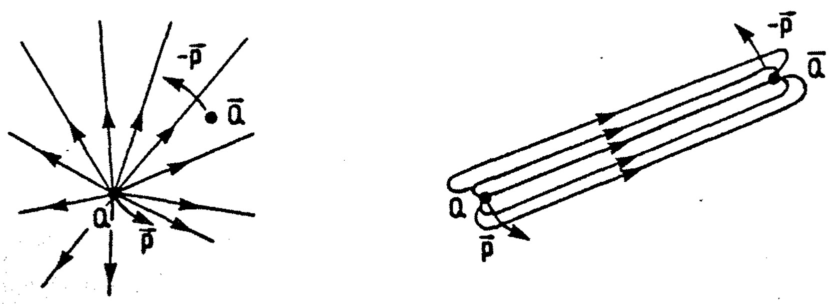

Figure 2: Field configurations determining the $q\bar{q}$ potential at small and large distances, from [9].

In the Richardson model the coordinate space potential V(r) is constructed by Fourier transforming the single dressed gluon exchange amplitude

$$V(q^2) = 4/3\,\alpha_s(q^2)/q^2$$

where $\alpha_s(q^2)$ is the running strong coupling constant. Asymptotic freedom and linear quark confinement are incorperated by requiring:

$$\alpha_s(q^2) \sim 12\pi/(33-2n_f)\ 1/\ln(-q^2/\Lambda^2)\quad,\text{ for } -q^2 \gg \lambda^2,\ \text{(asymptotic freedom)}$$

where n_f is the number of quark flavours and Λ is a scale parameter

$$V(r) \sim \text{const} \times r \quad , \text{for } r \gg 1/\Lambda \quad \text{(linear confinement)}$$

or equivalently

$$V(q^2) \sim \text{const} \times 1/(q^2)^2 \quad , \text{for } -q^2 \ll \Lambda^2$$

The interpolating formula incorporating these constraints is:

$$V(q^2) = -4/3 \; 12\pi/(33-2n_f) \; 1/q^2 \; 1/\ln(1+q^2/\Lambda^2)$$

This potential depends only on one single parameter, the scale Λ.

2. The other class of models try to describe quarkonium using simple empirical potentials. The Martin potential [10]

$$V(r) = A + B\, r^{\nu} \quad , A \text{ and } B \text{ parameters, and } \nu = 0.1$$

and the logarithmic potential [11]

$$V(r) = C \ln r/r_0 \quad , C \text{ and } r_0 \text{ parameters}$$

are two such examples.

We note that none of these models incorporate spin-dependent forces.

1.2.3 SPIN-DEPENDENT FORCES

There are several sophisticated methods to obtain the fine structure (e.g. ${}^3P_{0,1,2}$ mass differences) and the hyperfine structure (e.g. ${}^3S_1 - {}^1S_0$ mass difference) for quarkonia. See [21], [22], [24] and [23]. One of the more transparent ones are given in [14]. The structure of spin-dependent forces in heavy quark systems is predicted by applying the flux tube picture of electric confinement. This picture also led to the Coulomb plus linear potential model.

The spin-dependent interaction energy ΔE is given by

$$\Delta E = \Delta E_{ms} + \Delta E_{LS}$$

where ΔE_{LS} is the kinematic term due to the magnetic fields induced by the motion of the two particles and the magnetostatic energy ΔE_{ms} is:

$$\Delta E_{ms} = \Delta E_{SS} + \Delta E_T$$

where

$$\Delta E_{SS} = 8\pi/3\ (\alpha/m_1m_2)\ \vec{s_1}\cdot\vec{s_2}\ \delta^3(\vec{r}) \text{ ; spin-spin interaction energy}$$

$$\Delta E_T = (\alpha/m_1m_2)\ [3(\vec{s_1}\cdot\hat{r})(\vec{s_2}\cdot\hat{r}) - \vec{s_1}\cdot\vec{s_2}]\ 1/r^3 \text{ ; tensor interaction energy}$$

$\vec{s_i}$ and m_i are spin and mass of quark i and $\vec{r} = \vec{x_1} - \vec{x_2}$, $\hat{r} = \vec{r}/r$. For a derivation of these terms see [25]. Now

$$\Delta E_{LS} = -\mu_1\ \vec{s_1}\cdot\vec{B'}_{12} - \mu_2\ \vec{s_2}\cdot\vec{B'}_{21} + \vec{\omega_1}\cdot\vec{s_1} + \vec{\omega_2}\cdot\vec{s_2}$$

where $\mu_i = e_i/m_i$, $e_1 = -e_2 = e$ and $e^2 = 4\pi\alpha$. $\vec{B'}_{ij}$ is the magnetic field generated by particle j in the comoving rest frame of particle i. We have:

$$\vec{B'}_{ij} = -\vec{v}_{ij}\times\vec{E_j} \text{ (to the first order)}$$

where $\vec{v}_{ij}$ is the velocity of particle i relative to j and $\vec{E_j}$ is the static electric field generated by particle j in its own rest frame. In the case of a Coulomb potential we have:

$$\vec{E_j} = -1/e_j\ 1/r\ dV/dr\ \vec{r}_{ji}\ ,\ \vec{r}_{ji} = \vec{r_j} - \vec{r_i}$$

The vector $\vec{\omega_i}$ is the Thomas precession frequency of particle i:

$$\vec{\omega_i} = -1/2\ \vec{L}/m_i^2\ 1/r\ dV/dr$$

where

$$\vec{L} = \vec{r}_{ij}\times\vec{v}_{ij}m \quad ; m=m_1m_2/(m_1+m_2)$$

Now introducing a Coulomb potential $V(r) = -\alpha/r$ for the one gluon exchange in the quark-antiquark interactions at short distances, and a linear term $V(r) = kr$, and noticing that at large distances only the Thomas precession terms contribute, the complete Hamiltonian of spin-dependent forces can be written down with the substitution $\alpha \rightarrow 4/3\ \alpha_s$:

$$\Delta E = -(1/2\ \vec{L}\cdot\vec{s_1}/m_1^2 + 1/2\ \vec{L}\cdot\vec{s_2}/m_2^2)\ k/r$$

$$+ [1/2\ \vec{L}\cdot\vec{s_1}/m_1^2 + 1/2\ \vec{L}\cdot\vec{s_2}/m_2^2 + \vec{L}\cdot\vec{S}/m_1m_2]\ 4/3\ \alpha_s/r^3$$

$$+ 32\pi/9\ (\alpha_s/m_1m_2)\ \vec{s_1}\cdot\vec{s_2}\ \delta^3(\vec{r})$$

$$+ 4/3\ (\alpha_s/m_1m_2)\ [3(\vec{s_1}\cdot\hat{r})\ (\vec{s_2}\cdot\hat{r}) - \vec{s_1}\cdot\vec{s_2}]\ 1/r^3$$

where $\vec{S} = \vec{s_1} + \vec{s_2}$. The reasons that only the Thomas precession terms contribute at large distances are:

1. That the hypothesis of electric confinement states that at large distances the fields in flux tube at rest are purely electric. Thus none contributions from large distances to the magnetostatic energy.

2. The magnetic fields $\vec{B}'_{ij}$ in the comoving rest frames of the quark and the antiquark is zero at large distances.

The numerical results obtained by [14] using this formula for Δ E are given in table 1 . The different charmonium states below threshold are given in fig. 3 .

1.2.4 CHARMONIUM ANNIHILATION

The minimum number of gluons in the intermediate state of hadronic charmonium decay is determined by conservation laws (see [16] for a detailed discussion). Especially it is impossible for any charmonium state to decay into one gluon because of coulor conservation (hadrons are singlets under $SU_c(3)$ while gluons are components of an octet). The photonic annihilation of charmonium follows the conservation of J^{PC}. The different annihilation channels are given in table 2.
We note that the width of the $^3S_1$, $^1P_1$ and $^3P_1$ should be narrower than the other states because of the absence of the two−gluon and the two−photon decay.

The calculation of annihilation rates in QED and QCD are rather similar to each other to the lowest order in perturbation theory. There we consider only decays into the minimal number of gluons and therefore it is no place for a nonlinear coupling of gluons. Hence the calculated widths for the different positronium levels can be directly coupled to the charmonium widths:

$$\Gamma(^1S_0 \rightarrow 2\gamma) = 3\, e_c^4 \times \Gamma(e^+ e^- \rightarrow 2\gamma) \quad ,e_c = 2/3, \text{ charm quark charge}$$

$$\Gamma(^3S_1 \rightarrow 3\gamma) = 3\, e_c^6 \times \Gamma(e^+ e^- \rightarrow 3\gamma)$$

$$\Gamma(^3P_0 \rightarrow 2\gamma) = 3\, e_c^4 \times \Gamma(e^+ e^- \rightarrow 2\gamma)$$

$$\Gamma(^3P_2 \rightarrow 2\gamma) = 3\, e_c^4 \times \Gamma(e^+ e^- \rightarrow 2\gamma)$$

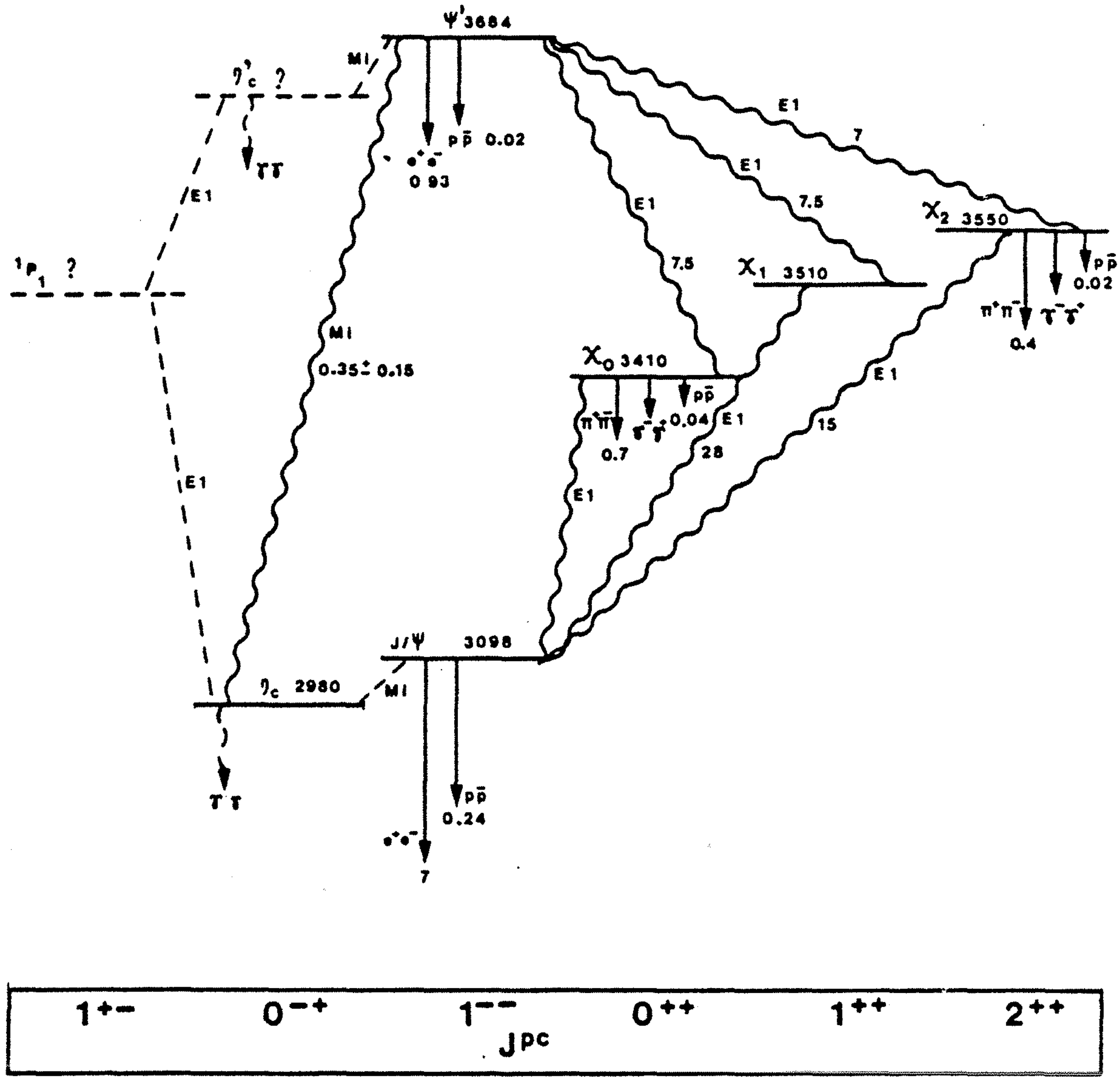

Figure 3: The charmonium spectrum.

$$\Gamma(^1S_0 \rightarrow 2\gamma) = 2/3\ \alpha_s^2/\alpha^2 \times \Gamma(e^+ e^- \rightarrow 2\gamma)$$

$$\Gamma(^3S_1 \rightarrow (3g)_d) = 5/18\ \alpha_s^3/\alpha^3 \times \Gamma(e^+ e^- \rightarrow 3\gamma)$$

$$\Gamma(^3P_0 \rightarrow 2g) = 2/3\ \alpha_s^2/\alpha^2 \times \Gamma(e^+ e^- \rightarrow 2\gamma)$$

and for the gluonic and photonic annihilations

$$\Gamma(c\bar{c} \rightarrow 2g) = 2/9e_c^4\ \alpha_s^2/\alpha^2 \times \Gamma(c\bar{c} \rightarrow 2\gamma)$$

$$\Gamma(c\bar{c} \rightarrow (3g)_d) = 5/54e_c^6\ \alpha_s^3/\alpha^3 \times \Gamma(c\bar{c} \rightarrow 3\gamma)$$

Table 1: Facts about charmonium below threshold.

State			Γ_{tot}(MeV)	m_{exp}(MeV)	Buchmuller
1^1S_0	η_c	0^{-+}	11.5 ± 4.5^a	2984 ± 6^a	
1^3S_1	J/ψ	1^{--}	0.063 ± 0.09^d	3096.93 ± 0.09^b	input
1^1P_1	$^1P_1$	1^{+-}		3525.8 ± 1.0^c	3521
1^3P_0	χ_0	0^{++}	$(0.85-4.9)^a$	3417.8 ± 4.0^a	3419
1^3P_1	χ_1	1^{++}	$< 1.3^a$	3511.3 ± 0.6^c	3502
1^3P_2	χ_2	2^{++}	2.6 ± 1.4^c	3557.8 ± 0.9^c	3553
2^1S_0	η'_c	0^{-+}	$< 7^a$	3591.5 ± 5.0^a	
2^3S_1	ψ'	1^{--}	0.215 ± 0.04^d	3686.0 ± 0.1^d	

a. From [13].
b. From [26].
c. From R704, to be published.
d. FROM [6].

Table 2: Coupling of different charmonium states to photons and gluons. The d and f indicate the type of coupling in coulor space, d (f) representing the symmetric (antisymmetric) coupling under permutations of the gluons. From [16].

Charmonium state	$^1S_0$	$^3S_1$	$^1P_1$	$^3P_0$	$^3P_1$	$^3P_2$
J^{PC}	0^{-+}	1^{--}	1^{+-}	0^{++}	1^{++}	2^{++}
Hadronic annihilation	2g	$(3g)_d$	$(3g)_d$	2g	$(3g)_f$/ $gq\bar{q}$	2g
Photonic annhilation	2γ	3γ	3γ	2γ	$4\gamma/\gamma q\bar{q}$	2γ

For the $^1P_1$ and the $^3P_1$ state the calculations are much more difficult and the devoted reader is invited to study [16] for both these calculations and the above expressions.

The expectional small width of the charmonium states below threshold is explained by the OZI−rule [20]. Charm is a quantity conserved in strong interactions. Thus one would anticipate the decay of charmonium

$$c\bar{c} \to c\bar{q} + \bar{c}q$$

where q = u, d or s. Hence if the physical $c\bar{q}$ states are heavier than $1/2\, m_{c\bar{c}}$, the hadronic decays can proceed only via disconnected diagrams, fig. 4 , and are therefore suppressed. This is true for all $c\bar{c}$ states up to ψ'. E.g the full width of ψ'' is $\Gamma_{\psi''}$ = 52 MeV (above threshold) to be compared with Γ_{ψ} = 0.063 MeV (below threshold).

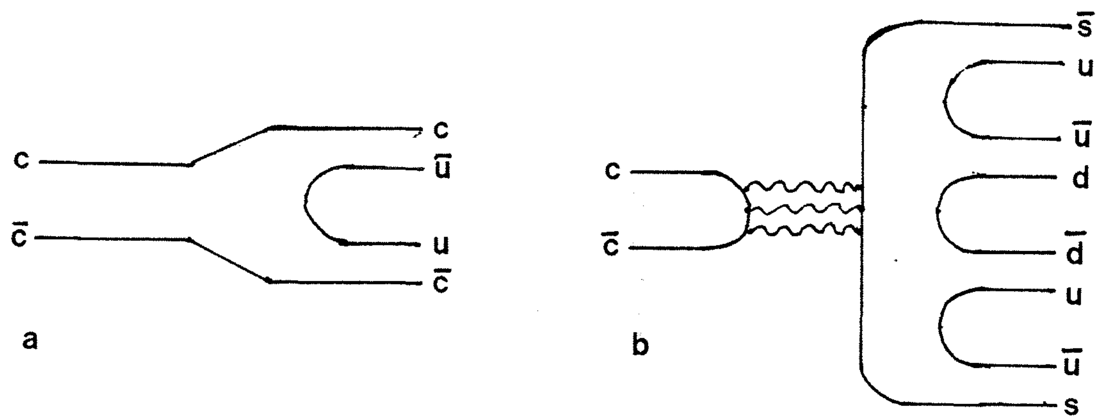

Figure 4: Connected and disconnected diagrams in $c\bar{c}$ annihilation.
a: $\psi'' \to D\bar{D}$ above threshold
b: $\psi \to K^+K^-\pi^+\pi^-$ (e.g. uncharmed hadrons), below threshold.

In QCD, the theory of strong interactions, the OZI−suppression is viewed in terms of a multigluon intermediate state, providing a well defined mechanism for violating the OZI−rule.

1.3 THE EXPERIMENTAL SITUATION

Most of the experimental data on charmonium states come from e^+e^- storage ring experiments (CRYSTAL BALL at SPEAR, MARK II at SPEAR, DORIS (the DASP collaboration) at DESY, VEPP−4 Novosibirsk etc.). In these experiments only states with the J^{PC} quantum numbers of the photon (1^{--}) can be produced directly, that is the J/ψ and its radial excitations, see fig. 5 .

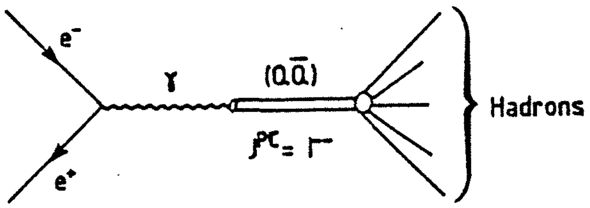

Figure 5: The production of charmonium in e^+e^- storage ring experiment.

Hence their mass and width have been measured with great precision and their different decay channels extensively studied. In these machines the χ states have been established by studying the decay of the $\psi' \to \gamma\,\chi$, and then search for monochromatic components of the inclusive γ spectrum, see fig. 6, or by studying the final state $\gamma\,\gamma\,J/\psi$ to test

its compability with the decay chain $\psi' \to \gamma\,\chi \to \gamma\,\gamma\,J/\psi$, where $J/\psi \to e^+e^-$ or $J/\psi \to \mu^+\mu^-$. Finally it has been found by studying hadronic final states in coincidence with a monochromatic γ−ray in the process $\psi' \to \gamma\,\chi \to \gamma$ + hadrons. The mass values of the χ states can thus be measured with reasonable precision. Values for the widths can be obtained from the inclusive γ−spectrum. The η_c state has been seen in the decay

$$\psi' \to \gamma\,\eta_c$$

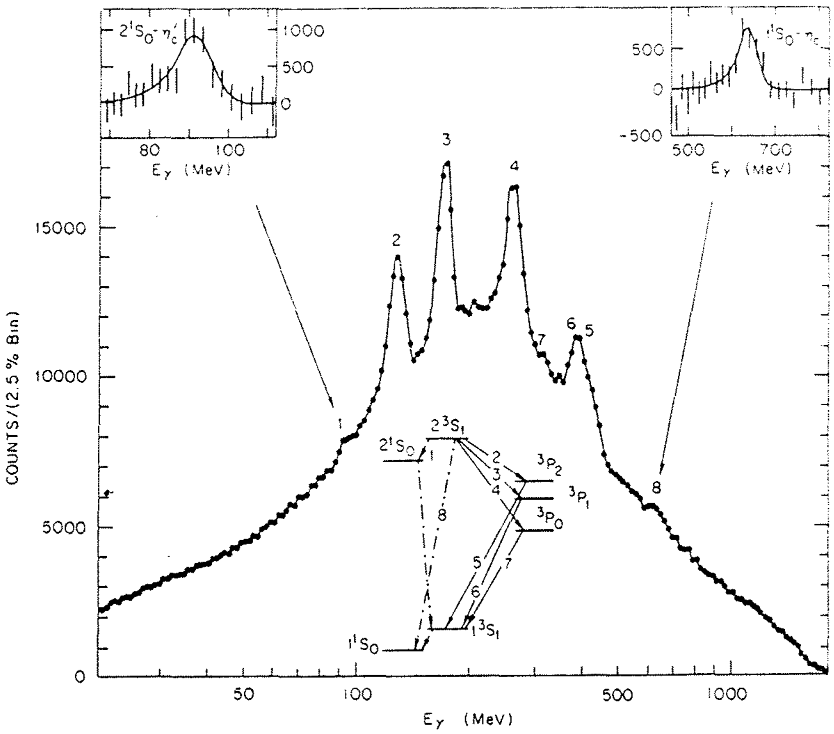

Figure 6: The inclusive γ – spectrum from Crystal Ball [27].

The same is true for the $\eta_c{}'$ state. The charmonium state $^1P_1$ have never been detected. It is predicted below charm threshold (see table 1) and should therefore be narrow. In e^+e^- – machines the $^1P_1$ can be seen only in the decay of the ψ' state. Single photon transitions between the ψ' and the $^1P_1$ states are forbidden by C conservation and so one must investigate double photon transitions. Crystal Ball has searched for a monochromatic π^0 in the decay

$$\psi' \rightarrow \pi^0 \; J/\psi$$

but the result was negative [27].

To gain more knowledge about the charmonium spectrum one can turn to 2 γ processes which unfortunately have small cross – sections or to hadronic processes.

In the annihilation of $p\bar{p}$ all charmonium states can be produced directly with an CMS energy set at $\sqrt{s} = m_R$, the resonance mass. Given a good momentum resolution ($\Delta p/p = \pm 4.0 \times 10^{-4}$) precise measurements of the widths can be done by doing a scan over the resonance mass.

An experiment (R704 at CERN's ISR) made use of this new technique to study charmonium states with $J^{PC} \neq 1$. This was made possible due to the antiproton facilities available at CERN. In the next section this experiment will be described, followed by the analysis of the χ_1 state and the values obtained for the mass, the total width, the partial width $\Gamma_{p\bar{p}}$ and the $Br(\chi_1 \rightarrow p\bar{p})$ of the χ_1 state.

2. R704, THE EXPERIMENTAL SET – UP

2.1 INTRODUCTION

The R704 was a formation[2] experiment. With a $p\bar{p}$ initial state, all charmonium states could be formed directly. The antiprotons were provided by the AA (Antiproton Accumulator). After being cooled down they were transferred to the ISR (Intersecting Storage Rings). On the ring a hydrogen jet target was installed. The H_2 – molecule flux across the beam gave a proton target that was dense enough to provide the luminosity required for the experiment to be successful and that did not blow up the antiproton beam too much. Thus it was possible to keep the antiprotons in the ISR for several days.

The detector consisted of two arms surrounded by guard detectors and was designed to detect electro-magnetic final states. This to avoid the huge (70 mb) non – resonant hadronic background.

Below a short description of the experimental set – up is given. For more details see [29].

2.2 THE BEAM

The antiprotons were produced by bombarding a tungsten target with 26 GeV/c protons from the proton synchrotron (PS). They were accumulated in the AA with a momentum of 3.5 GeV/c. The AA stack was ejected in two or three large slices. After ejection the bunch made half a turn inside the PS before being immediately injected to ring 2 of the ISR (fig 7). The final stack was made by phase displacing the first pulse away from the injection orbit, injecting the second pulse and then momentum cooling the two pulses together. This process was then repeated in the case of a third pulse. The transfer efficiency from the AA to the ISR was normally 65 – 75% at 3.5 GeV/c. From a stack of $\geq 2\times 10^{11}$ antiprotons in the AA it was thus possible to obtain 5 – 6mA ($1 - 1.2\times 10^{11}$ particles) of antiprotons for physics in the ISR.

---

[2] In a formation experiment, the resonant state is formed by combination of the colliding particles, at a Center of Mass energy just equal to the mass of the resonant state.

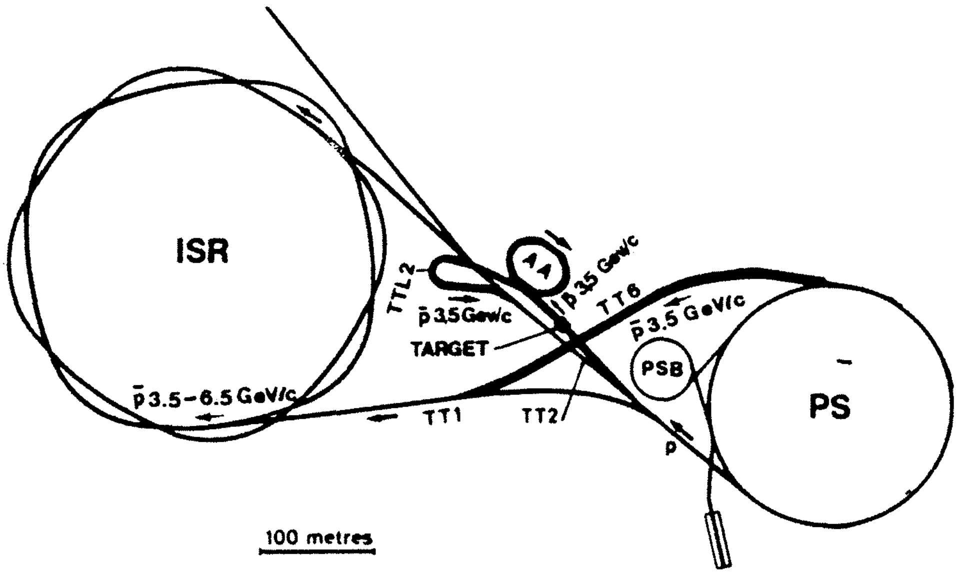

Figure 7: Layout of AA − PS − ISR and beam transfer lines. From [29].

The beam momentum could be varied between 3.6 GeV/c (η_c) and 5.7 GeV/c (χ_2). The ISR RF system was used for larger steps (minimum momentum step 3 − 6 GeV/c), while for smaller step, ~ 1 MeV/c, the momentum cooling system was used. By applying a small local radial bump in the momentum cooling pick − up, the beam was no longer centered and the cooling system would then accelerate or decelerate the beam depending on the sign of the bump, to get it back on center. By using this method of stochastic acceleration the beam momentum could be very fined tuned.

To counteract the blow up of the antiproton beam and momentum degradation due to the repeated passages through the dense jet of hydrogen gas, the ISR's stochastic cooling systems were used. The cooling systems were also important in reducing the momentum spread, and a $\Delta p/p < 4 \times 10^{-4}$ was obtained.

The absolute measurement of the beam momentum was of prime importance as this measurement determined the final errors in the particles mass determination. The beam momentum measurement was done in two different ways:

i. With bunched beam, by measuring the closed orbit (l_{ISR}) and the revolution frequency (ν) the particles velocity could be found and hence the momentum using:

$\beta = l_{ISR}\nu/c$

$p/m_0 c = \beta\gamma$

where

l_{ISR} = ISR orbit length = 942.56073 m

$1/\nu$ = 3.250495 μs

β = 0.9672597

which gives p = 3.5756 GeV/c. We have:

$$\Delta p/p = \gamma^2 \, \Delta\beta/\beta$$

and

$$\Delta\beta/\beta = \sqrt{(\Delta l_{ISR}/l_{ISR})^2 + (\Delta\nu/\nu)^2}$$

The errors on the momentum measurement:

$\Delta l_{ISR}/l_{ISR} = \pm 3.6\times 10^{-6}$

$\Delta\nu/\nu = \pm 2.5\times 10^{-6}$

which gives $\Delta p/p = \pm 0.7\times 10^{-4}$ or $\Delta p = \pm 250$ keV/c.

ii. With debunched beams by measuring the magnetic field (B). The momentum p is then given by $p = k\int B\, dl$, where k is a constant. The magnetic field measurement was done in two different ways. One was by using a Hall probe and the other by a flipping coil device[3]. The results of all measurements are given in table 3 .

After a full calibration of the ISR magnetic field measuring system it was possible to determine the beam momentum to within 1 MeV/c and thus have a mass resolution of $\leq$300 keV. The results obtained from the process $p\bar{p}\rightarrow J/\psi\rightarrow e^+e^-$ confirm this[4]. The R704 data gives

[3] For a description of the Hall probe and the flipping coil methods see [38].

[4] The detection of the J/ψ was a key item for the experiment, for establishing the success of the method and for giving a means of checking the ISR momentum calibration and reproducibility and to provide a bank of events to check detector perform-

Table 3: Results from the momentum calibration. From [29].

Absolute calibration	3.5756 ± 0.001	GeV/c
Hall probe	3.576 ± 0.002	GeV/c
Flip coil	3.5745 ± 0.002	GeV/c
Given by PS/AA	3.575	GeV/c

$m_{J/\psi} = (3096.92 \pm 0.1 \pm 0.27)$ MeV/c^2 where the first (second) error is statistical (systematic), to be compared with the Novosibirsk data $m_{J/\psi}$ = (3096.93 ± 0.09) MeV/c^2 [32].

2.3 THE H_2 GAS JET TARGET

The internal gas target was obtained using a beam of clusters of hydrogen molecules which crossed the antiproton beam perpendicularly (fig 8 and 9). Expanding H_2 at high pressure ($p_0 =$ 10 bar) and low temperature ($T_0 =$ 77 K) through an injector of special geometry and a very small throat (fig 10), gave a H_2 flux with good properties as an internal target in a storage ring [30].

To avoid pressure rise in the interaction region, the central part of the flux was absorbed by the sink pump system after passing across ISR ring 2 (fig 11).

The target thickness obtained on the path of the antiproton beam was 10^{14} atoms per square centimetre. The luminosity can be expressed as:

$$L = \rho n \upsilon$$

ρ = density of atoms $\sim 10^{14}$ atoms cm^{-2}

υ = revolution frequency $\sim 0.97c/l_{\mathrm{ISR}} \cong 3.0\times 10^{30}$ s^{-1}

ances and.to set software cuts for the other analysises. For more details see [31].

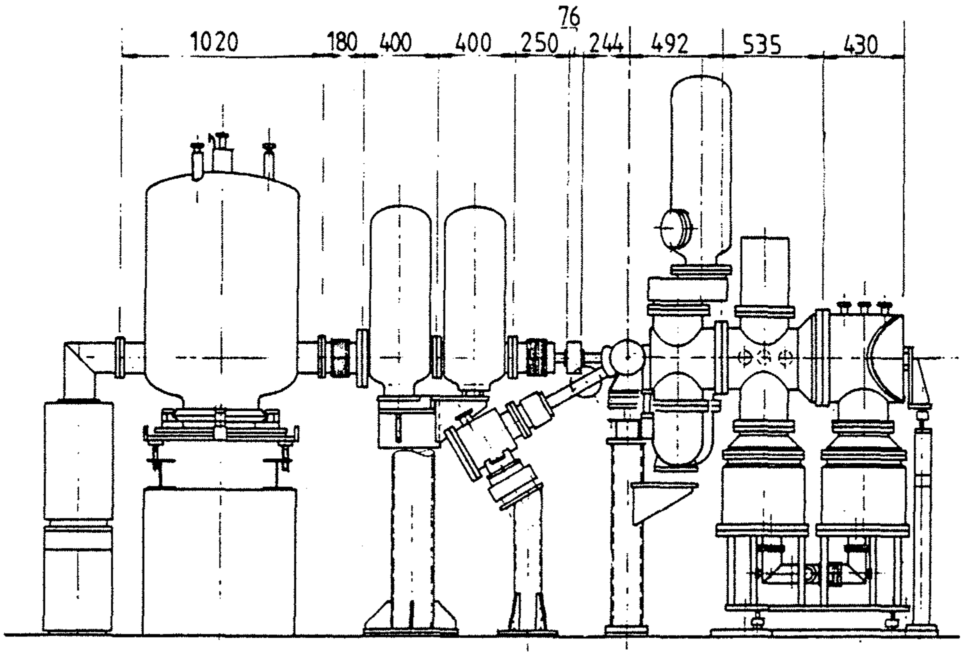

Figure 8: Schematic front view of the target system. From [29].

n = number of $\bar{p}$ in the ISR $\sim 1.2\times 10^{11}$

which gives: $L \cong 3.6\times 10^{30}\ cm^{-2}\ s^{-1}$

The maximum luminosity actually obtained was $3.0\times 10^{30}\ cm^{-2}\ s^{-1}$.

It was important that the H_2 jet target did not blow up the $\bar{p}$ − beam to much. The antiprotons are lost if they undergo

i. elastic scattering at larger angles than the machine acceptance

ii. inelastic reactions

The intensity of the circulating $\bar{p}$ − beam is given by:

$$I = I_0 \exp(-\sigma\rho v t)$$

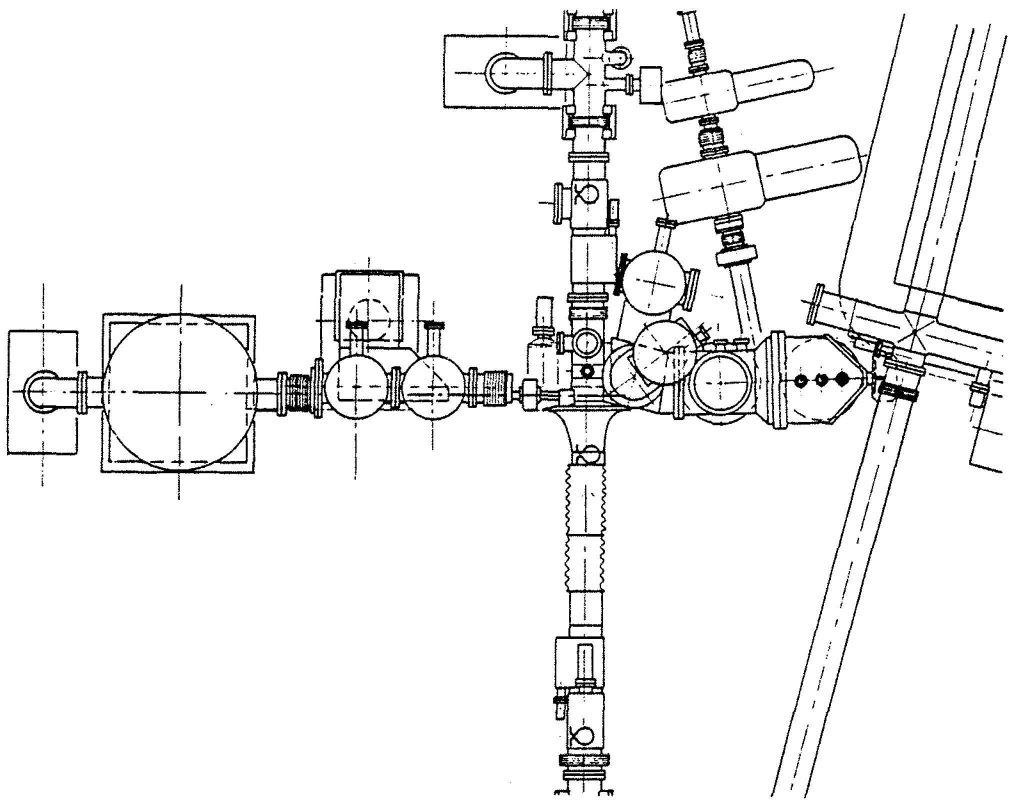

Figure 9: Schematic top view of the target system. From [29].

where I_0 is the initial intensity of the $\bar{p}$-beam, ν the revolution frequency, ρ the density of the jet (atoms/cm^2) and t the time the $\bar{p}$-beam has been in the ring with the jet on. $\sigma = \sigma_{el}(>\theta_0) + \sigma_{inel}$ where θ_0 is the rings acceptance level.

For the χ_1-run period (22.05.84 − 27.05.84) the initial luminosity was 5.2236 mA. After ~130 hours in the ring 1.237 mA (23 %) of the $\bar{p}$-beam was still left.

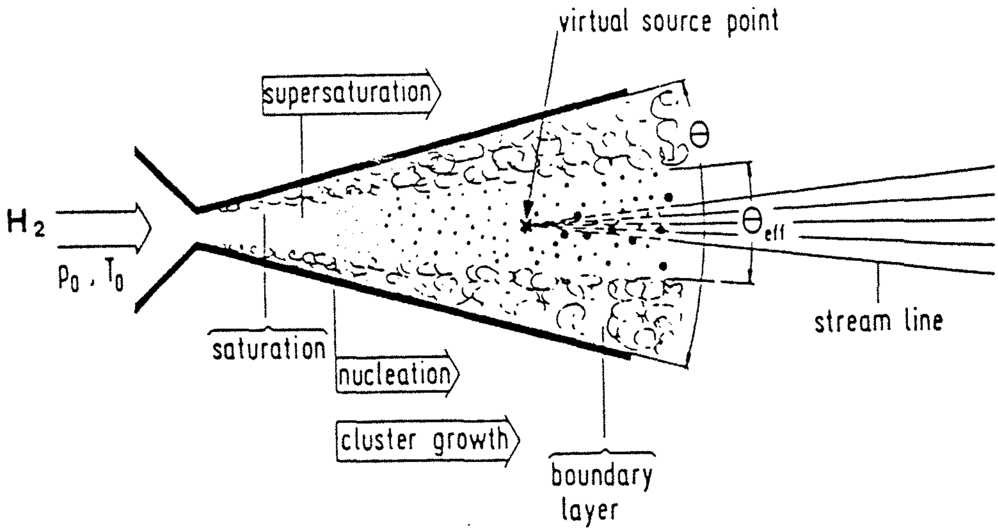

Figure 10: Converging – diverging nozzle. The location of the different phases of the gas expansion is indicated. From [29].

2.4 THE DETECTOR

To minimize the problems from the huge ($\sigma \cong 70$ mb) non – resonant hadronic background the detector was designed to detect electromagnetic decays of the charmonium states:

$$p\bar{p} \rightarrow J/\psi \rightarrow e^+e^-$$

$$p\bar{p} \rightarrow \chi_1, \chi_2 \rightarrow J/\psi\,\gamma \rightarrow e^+e^-\gamma$$

$$p\bar{p} \rightarrow \eta_c \rightarrow \gamma\gamma$$

The detector consisted of two arms (left – right, fig 12) surrounded by guard detectors. Each arm had a trapezoidal shape following the θ, ϕ acceptance in the lab system. θ_{lab} varied between 17 ° and 66 ° and $\Delta\phi$ = 45 °. Charged and neutral guard detectors covered a large part of the remaining solid angle. The overall acceptance was ~12% for e^+e^- or $\gamma\gamma$ and ~10% for $e^+e^-\gamma$ final states.

Each arm was made of a charged telescope and an electromagnetic calorimeter (fig 13).

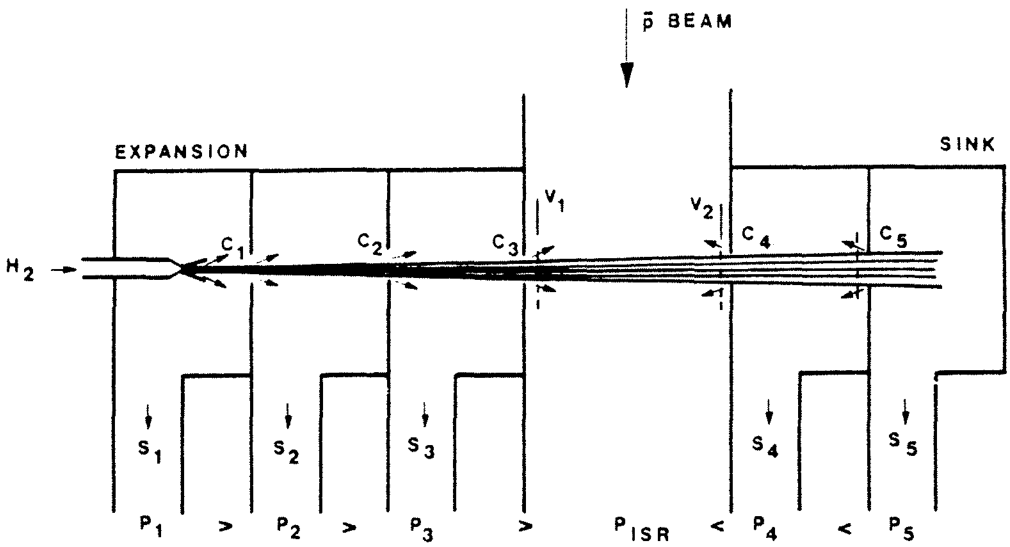

Stage	S (ℓ/s)	C (ℓ/s)
1	7000	0.7
2	4000	3.0
3	4000	7.0
ISR	2000	80.0
4	S4=8000	1100.0
5	S5=120000	

Figure 11: Schematic of the target system : chambers 1, 2, 3 production, chambers 4, 5 sink; the gas beam crosses the antiproton beam at 90°. Pumping speed for each stage and conductances between chambers are listed. From [29].

2.4.1 THE CHARGED TELESCOPE

The charged telescope consisted of the following parts:

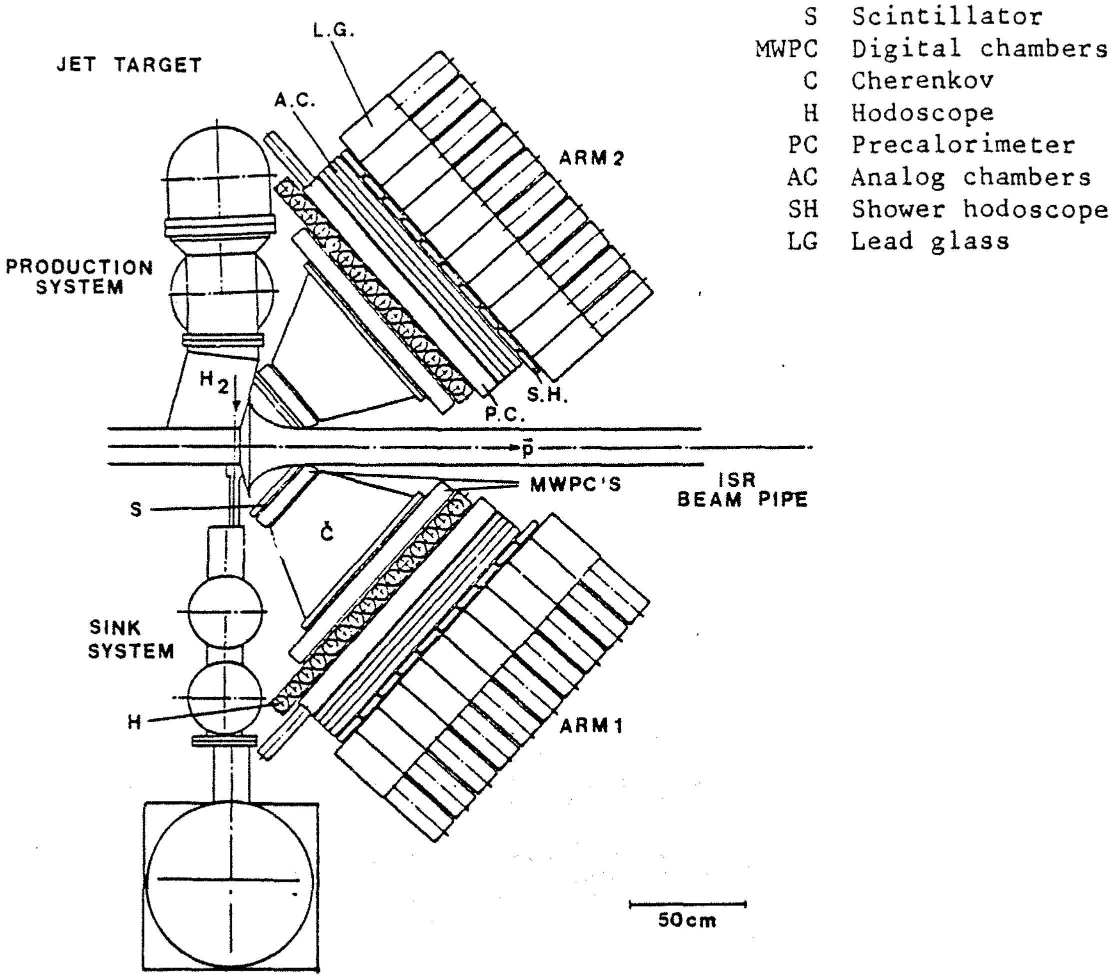

Figure 12: Top view of the two main arms and a part of the molecular H_2 jet system. The guard counters are not represented. From [29].

2.4.1.1 Scintillator hodoscopes (S and H) for the trigger.

The scintillator hodoscopes consisted of two sets of scintillator planes, S and H. S was simply a trapezoidal shaped scintillator counter 5 mm thick covering the whole acceptance. There was one in front of each arm at a distance of 290 mm from the vertex. H consisted of two planes of counters, $H\theta$ made of 10 vertical scintillator strips,87 mm wide and 10 mm thick, and $H\phi$ made of 6 wedge−shaped

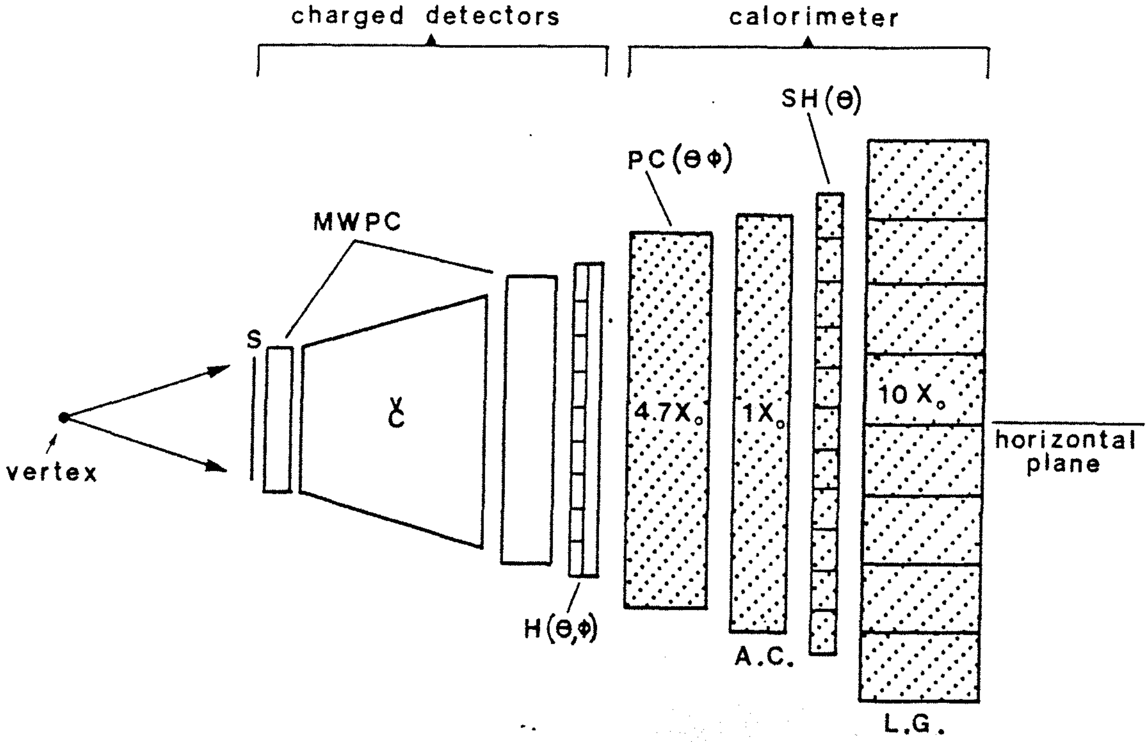

S	Scintillation counter
MWPC	3 planes (X,Y,V) digital chambers
C	Freon Cherenkov counter
H(θ,ϕ)	Charged hodoscope(θ,ϕ)
PC(θ,ϕ)	Precalorimeter
AC	Analog chambers
SH(θ)	Shower hodoscope(θ)
LG	Lead glass wall

Figure 13: Sketch of one main arm (not to scale). The charged detectors and the calorimeter are detailed. From [29].

scintillators 5 mm thick. It was placed behind the second MWPC. The signals from the S and H hodscopes were mainly used for for triggering purposes, but the S – hodoscope signal was also used in the offline analysis.

2.4.1.2 A threshold gas Cerenkov (C) counter to identify electrons.

The Cerenkov counters were used to distinguish electrons from pions. They were filled with freon − 13 at atmospheric pressure. The threshold was 0.013 GeV/c for electrons and 3.68 GeV/c for pions. The Cerenkov light was viewed by two photomultipliers and the average number of photoelectrons for an incident electron was $<N_{pe}> \cong 5.5$. The trigger required 1.5 photoelectrons . If it is assumed that the number of photoelectrons is Poisson distributed, a Cerenkov efficiency of 94 − 98% in each arm or totally ~93% is obtained. The Cerenkov signal was also used in the offline analysis, see chapter 3.

2.4.1.3 Multiwire Proportional Chambers (MWPC's)

The MWPC's were trapezoidal in shape. In each arm there were two chambers, placed at 300 mm and 825 mm from the interaction region. Each MWPC chamber was made of three planes X, Y and U with 2 mm pitch and 6 mm gap and filled with a mixture of argon (70%), isobutane (30%) and freon (0.3%), fig. 14. The readout was digital. The purpose of the MWPC was to reconstruct the tracks of charged particles. Requiring 5 or 6 plane solutions an efficiency of 95% per arm for reconstructing lines was obtained

[29]. The precision in the angle measurement was $\sigma_\theta = \sigma_\phi = 3-4$ mrad. A short description of how the MWPC's work is given in appendix A.

2.4.2 THE CALORIMETER

The role of the calorimeter was to measure the electron energy and improve on the electron/hadron discrimination. The analog chambers could also be used to accurately reconstruct track parameters from electron and photon initial showers. Each calorimeter had four parts of which two were used for the energy determination.

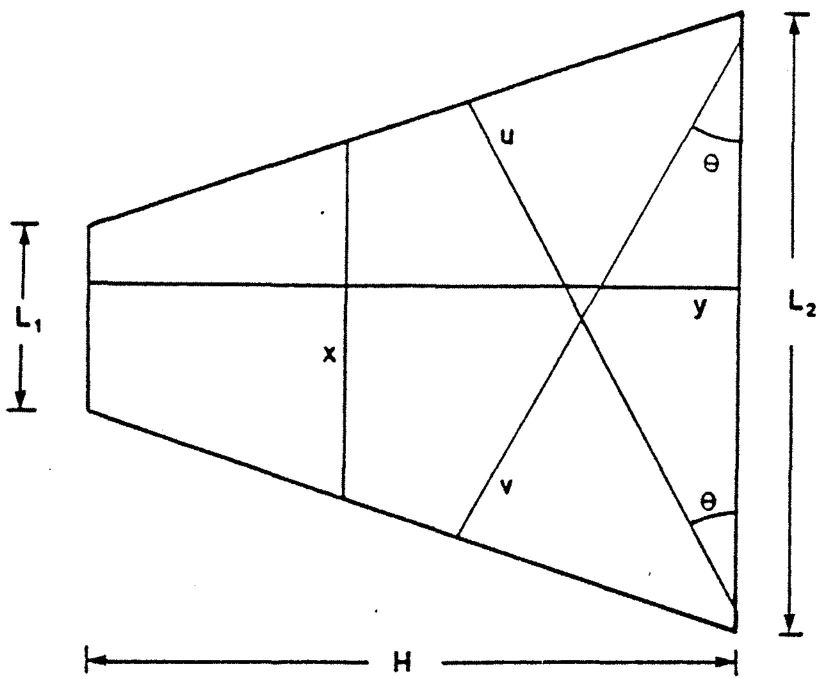

Figure 14: Orientation of the X,Y and U planes in the MWPC. $\theta = 28°$
Chamber 1:$L_1 = 140$ mm, $L_2 = 357$ mm, H = 350 mm.
Chamber 2:$L_1 = 460$ mm, $L_2 = 1117$ mm, H = 1059 mm.
From [31].

2.4.2.1 Precalorimeter, active in the energy measurement.

The precalorimeter had a depth of 4.7 X_0[5] and was made of lead−scintillator sandwiches. It consisted of 29 θ counters (vertical strips) and 14 ϕ counters (wedge−shaped strips) (fig 15). There were a total of 5 layers of θ counters and the same for the ϕ counters.The scintillators (NE110, 5 mm thick) were alternated in the sandwich with plates of lead (2.5 mm thick). The θ information of the five layers were viewed by one photomultiplier and same is true for the ϕ information, see fig 16.

The purposes of the precalorimeter were:

[5] X_0, radiation length, is that thickness of material in which a high energy electron loses all but a fraction 1/e of its energy to Bremsstrahlung, on average.

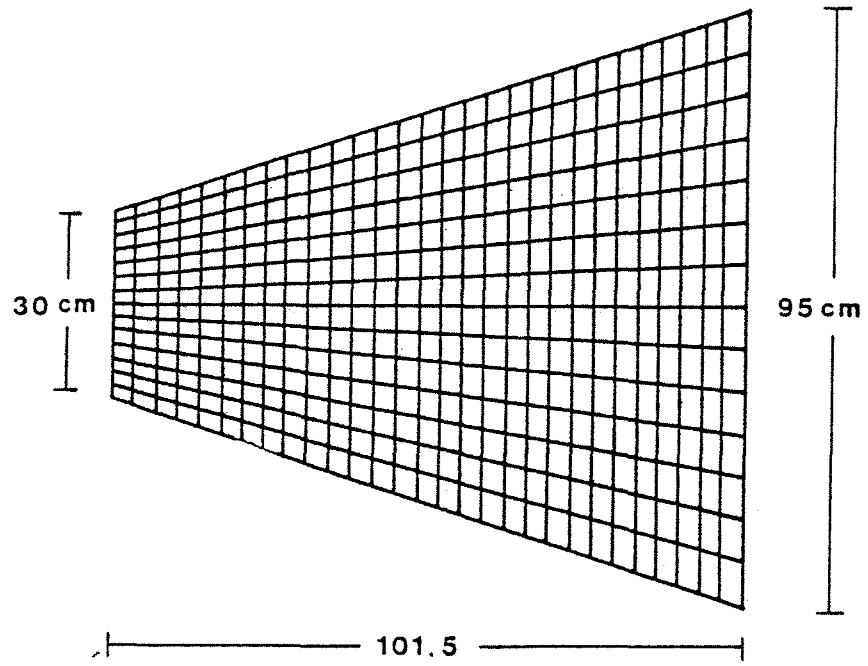

Figure 15: Front view of one precalorimeter consisting of 29 θ – counters (vertical) and 14 ϕ – counters (wedge – shaped). From [29].

- to separate 2γ from single γ showers
- to have a good detection efficiency for low energy γ's down to 50 MeV or even less in the case of asymmetric π^0 decays.
- to help measure the energy of the initial particle.

2.4.2.2 Analog chambers

The analog chambers were 1 X_0 deep and consisted of 4 identical (X,Y) chambers with analog readout of the cathodic strips. The anode planes of each chamber was made of 20 μm wires with 4 mm pitch. They were placed between 2 cathodic planes (X,Y) made of strips of copper – kapton printed – circuit foils (10 mm pitch, fig 17). Between each chamber a foil of lead (1mm thick) regenerated the shower

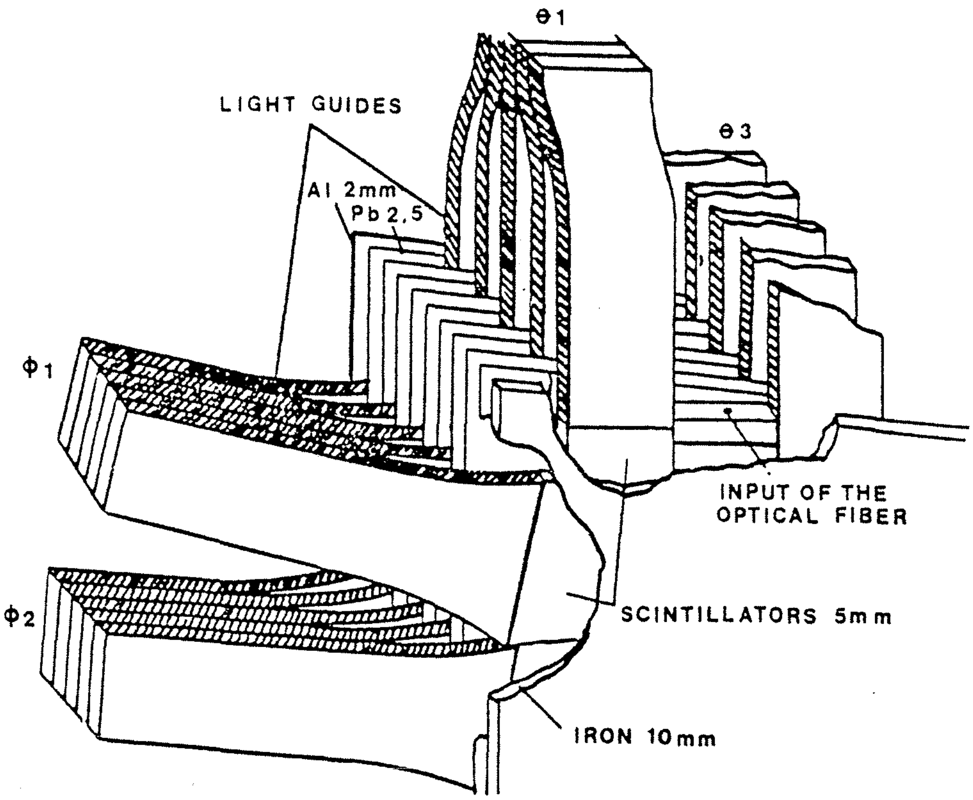

Figure 16: The arrangement of the scintillators of the precalorimeter. Five layers of NE110 are glued on a light-giude and define one counter. From [29].

core and absorbed low energy γ's and electrons. The aluminium plates (see fig 18) ensured rigidity and also had a quenching effect on very low energy electrons.

The roles of the analog chamber were:

- to avoid confusing a 2-shower π^0 event with a single γ
- to understand and visualize what happened in the case of difficult events: late conversion in the precalorimeter and high energy in the lead glass.
- to give the coordinates of the centre of gravity of the shower

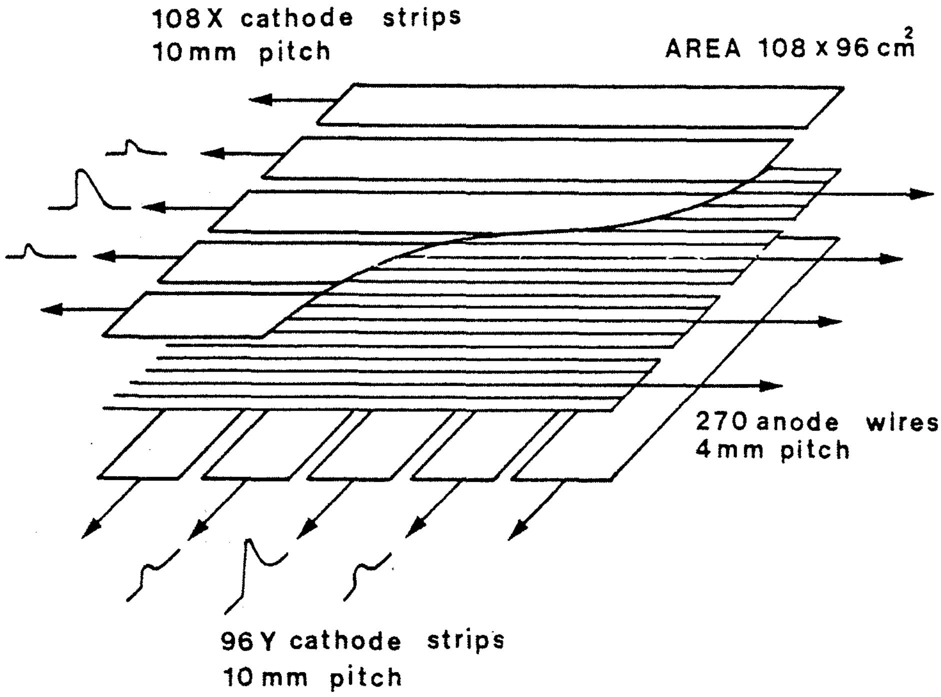

Figure 17: Main features of the design of one (X,Y) chamber. From [29].

- in case the MWPC's failed to reconstruct a track the information from the analog chambers could be used, thus giving a higher detection efficiency.

A short description of how the analog chambers work are given in appendix A.

2.4.2.3 Shower hodoscopes (SH) for triggering purposes

The shower hodoscope had a depth of 0.02 X_0 and was made of 14 vertical scintillator strips (NE110, 1 cm thick) and had triggering purposes.

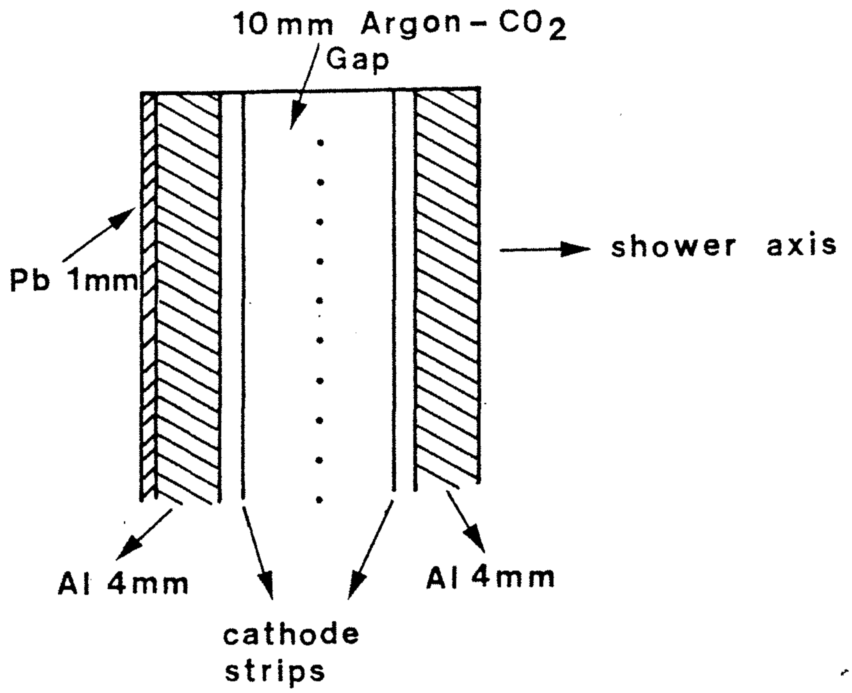

Figure 18: Structure of one (X,Y) analog chamber along the shower axis. From [29].

2.4.2.4 Lead Glass (LG) wall, active in the energy measurement

The LG was 10 X_0 deep. It consisted of a wall of 66 blocks of F2 glass from Schott, each with dimensions $15 \times 15 \times 30.5$ cm^3 (fig 19). Each block was viewed by a EMI 9928KA photomultiplier. The main role of the LG was to measure the remaining energy of the shower.

2.4.3 THE GUARD DETECTORS (THE VETO COUNTERS)

In order to detect exclusive two− or three−body reactions, it was necessary to cover a large solid angle. The guard detectors surrounded the two arms completely, covering most of the remaining solid angle, ranging from $\theta = 1.7°$ to $76°$ and a full azimuthal coverage. A system of 24 scintillation count-

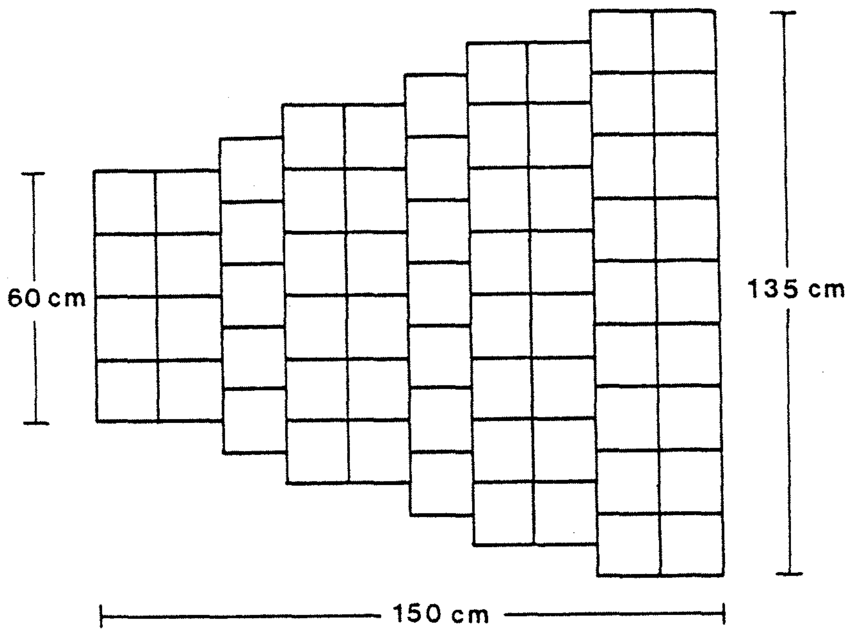

Figure 19: Front view of one of the lead glass walls. The arrangement consists of 66 blocks of F2 glass, 15×15×30.5 cm^3, from Schott. From [29].

ers detected charged particles while a set of 50 elements of lead – scintillator sandwich counters detected photons (fig 20). The vetoes were used to check what happened outside the two arms. For two – body final states there should be nothing in the vetoes, while for the three – body final state $e^+e^-\gamma$ the veto would detect the position of the single γ in the case it hit a veto counter.

2.5 LUMINOSITY MEASUREMENT

In order to be able to calculate any parameters of the states being searched for, a measure of the luminosity was needed. In R704 the calibration and monitoring of the luminosity was performed from small angle elastic scattering ($p\bar{p} \rightarrow p\bar{p}$) measurements. The elastic protons recoiling at large laboratory

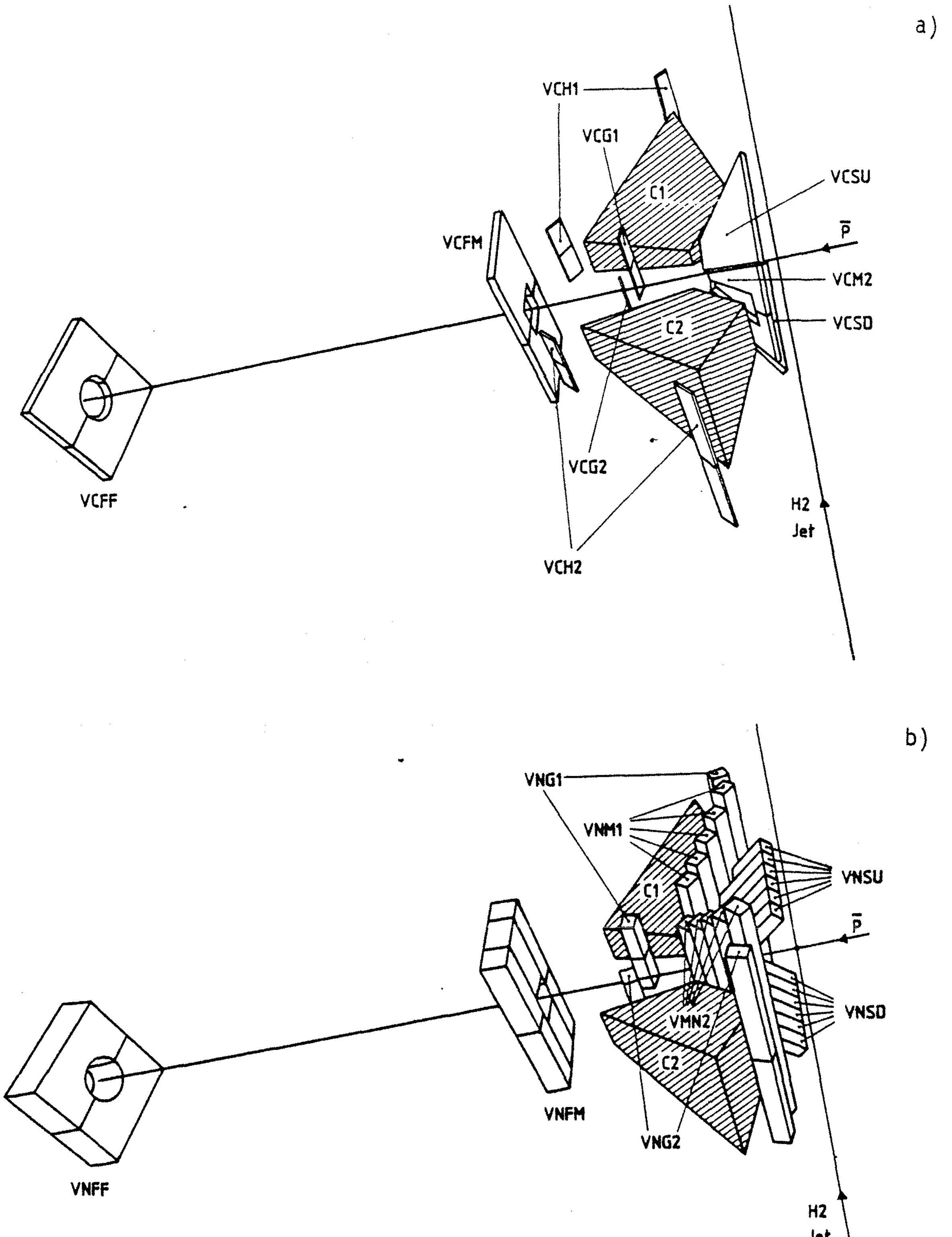

Figure 20: Sketch of the guard counters
a) charged vetoes V_c
b) neutral vetoes V_n From [29].

angles were detected and their kinetic energy measured with eight solid – state silicon detectors (fig 21). The number N of protons detected during a time ΔT in a range of momentum transfer squared Δt is given by:

$$N = A\, L\, \Delta T\, \Delta t\, d\sigma/dt$$

A being the acceptance of the detector

L the luminosity

$d\sigma/dt$ the $p\bar{p}$ elastic differential cross – section

The time integrated luminosity for each run is then given by:

$$L^{int}\, (d\sigma/dt) = N\, /(A\, \Delta t)$$

The data – acquisition system was based on a fast CAB μ – processor [37], providing acquisition, storage and readout of the detector spectra. It was under control of the central computer NORD 10 which wrote on tape at regular time intervals the content of the CAB memory and gave on line a value of the luminosity.

2.6 THE TRIGGER

The purpose of the trigger was to select in a very short time interesting events out of a huge background, such that only possible $c\bar{c}$ – candidates were written to tape.

The trigger had a three – level structure:

i. The first level T, lasting 50 ns, was a coincidence between hodoscope matrices ($MH\theta = H_1\theta \times H_2\theta$, $MH\phi = H_1\phi \times H_2\phi$, $MSH = SH_1 \times SH_2$, where $H_1\theta$ denotes element θ in hodoscope H, arm 1, etc.) programmed to correspond to the kinematics of the chosen trigger and a two arm coincidence with counters S_i and C_i, with additional constraints from guard counters, lifetime, monitors, etc. The logic was based on a programmable logic unit (PLU, LRS4508) under computer control. For example:

$$T_{e^+e^-} = MSH \times MH\theta \times MH\phi \times S_1 S_2 C_1 C_2 \times \bar{V}_c$$

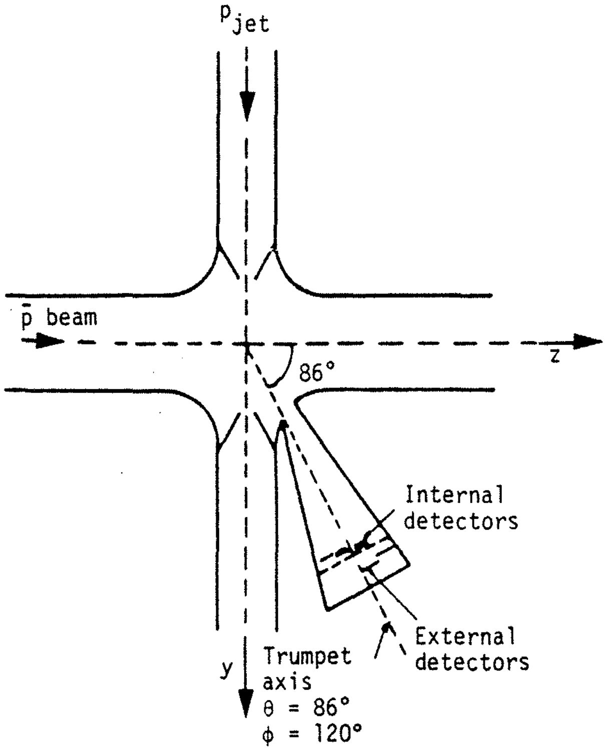

Figure 21: Experimental set − up of the luminosity detectors, top view. From [29].

ii. The second level, TT, lasted 200 ns and corresponded to selected multiplicities in each of the detector elements $H_1\theta$, $H_2\theta$, $H_{12}\ \phi$, SH_1, SH_2, V_c, V_n.

iii. The third level, TTT, which took 450 ns, used a fast CAB μ − processor, which read the fast ADC's, calculated the energy deposited in the precalorimeter and the lead glass and rejected events with an energy deposited less than a preset cut − value.

Three types of triggers were running simultaneously, T_1 = charged, T_2 = neutral and TM = monitor − trigger. The monitor − trigger was necessary to be able to on line test the stability of the energy calibration of the calorimeter. The acquisition rate was typically a few events per second for a luminosity $L = 10^{30}\ cm^{-2}\ s^{-1}$.

2.7 DATA ACQUISITION AND CONTROL

The general flow of data from CAMAC[6] modules to magnetic tapes was supervised by a NORD 10 computer. The information from the MWPC's were read out by a RMH[7] system (3500 digital channels) . A MICE[8] system spied on the RMH information read by the NORD 10 at CAMAC speed (MICE was ten times faster than CAMAC), and performed fast kinematical analysis and effective mass reconstruction (5 ms). In this way it was possible to get an on − line J/ψ − mass reconstruction which was useful for the mass − scanning operations. The NORD 10 functions were twofold:

i. Steering of the experiment (in order of decreasing priorities)

   - transfer data to magnetic tape
   - CAMAC readout
   - dispatch of data to sampling tasks

ii. Sample analysis. This was made by a comprehensive set of real − time tasks that run upon experimental team request and a real − time task that was always running for control of the most critical parts of the apparatus.

A sketch of the on − line system is given in fig 22.

2.8 SHORT SUMMARY

R704 was looking for bound states of charmonium. The experimental method was as follows: The antiproton beam hit the H_2 jet, the momentum of the circulating beam was adjusted in order to form the state under study and scan over its total width.

The main features of the experiment were:

---

[6] CAMAC is a standard system for connecting instruments to computers, see [36]

[7] RMH Receiver − Memory − Hybrid interface, see [33].

[8] MICE, a fast user − microprogrammable processor, see [34] and [35].

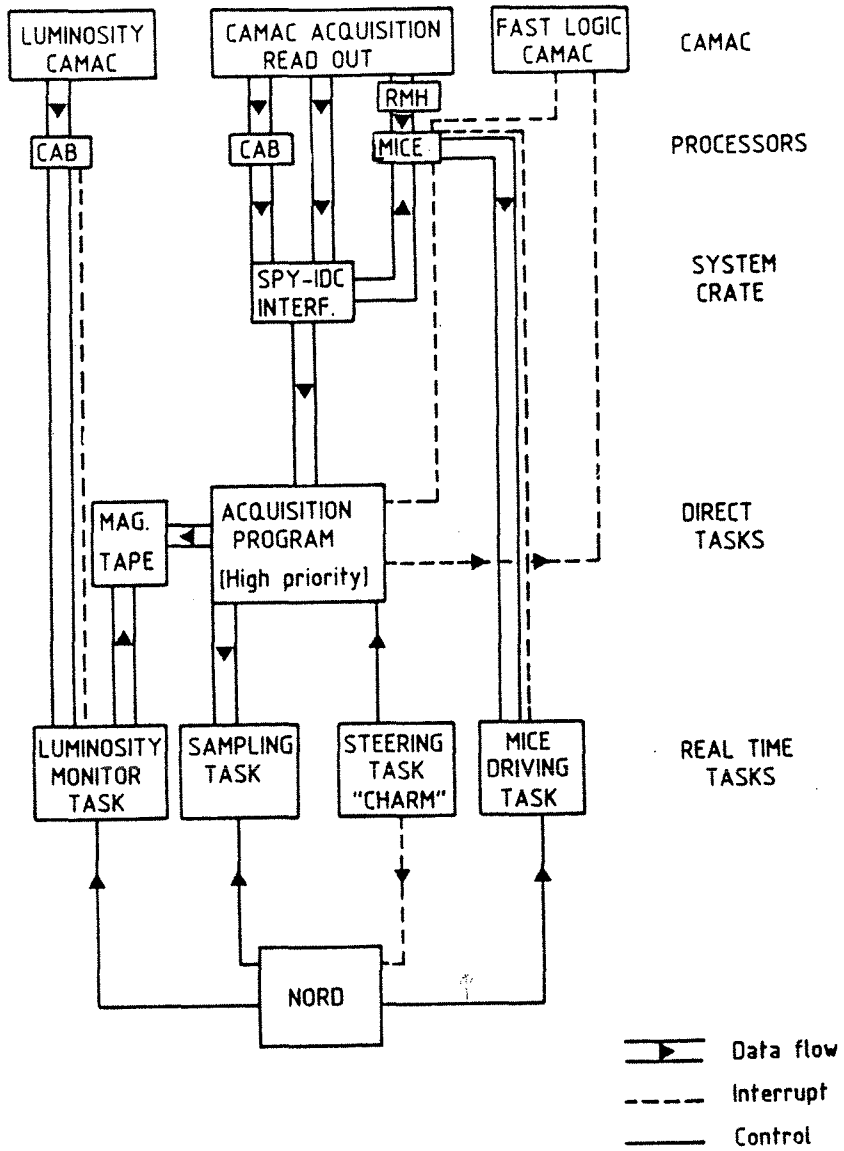

Figure 22: Summary of the on – line system. From [29].

- a luminosity larger than 10^{30} cm^{-2} s^{-1}
- an absolute energy calibration in the center of mass of the order of 300 keV

- the capability of sweeping continously through the resonance mass region with beam lifetimes of several days
- a detector capable of selecting the formation of charmonium states among a huge background of hadronic interactions, by focussing on purely electromagnetic final states

3. THE OFFLINE ANALYSIS

3.1 INTRODUCTION

The offline analysis is the last step on the way to find the events being searched for. The trigger selects those events which look promising, but still there is a large bakcground present. The aim of the offline analysis is to get rid of this background and keep the true events, or at least to produce a clear signal over an estimated background.

The offline analysis for the χ_1 state is described below[9]. It consists of two main parts, filtering (3.2) and the main analysis (3.3 − 3.7) . The analysis chain is given in fig. 23 .

In the process $p\bar{p} \rightarrow \chi_1 \rightarrow J/\psi\,\gamma \rightarrow e^+e^-\,\gamma$ the aim was to detect one electron in each arm. Then to follow the electron track through each detector arm, determine the energy deposited and calculate the invariant mass of the e^+e^- system using the simple formula:

$$m_{e^+e^-} = \sqrt{2\,E_1\,E_2\,(1-\cos\theta)}$$

$E_{1,2}$ = energy of electron, arm 1, 2

θ = angle between the two tracks (lab. system)

Requiring $m_{e^+e^-} > m_{cut}$ (production, section 3.4) , applying additional cuts on the signals deposited in different parts of the detector (section 3.5) and finally a kinematical check of the process (section 3.6) would eventually minimise the background and leave a final sample of accepted χ_1 events.

[9] In Oslo the same program was used for the analysis of the χ_2 state and the search for the singlet $^1P_1$ state.

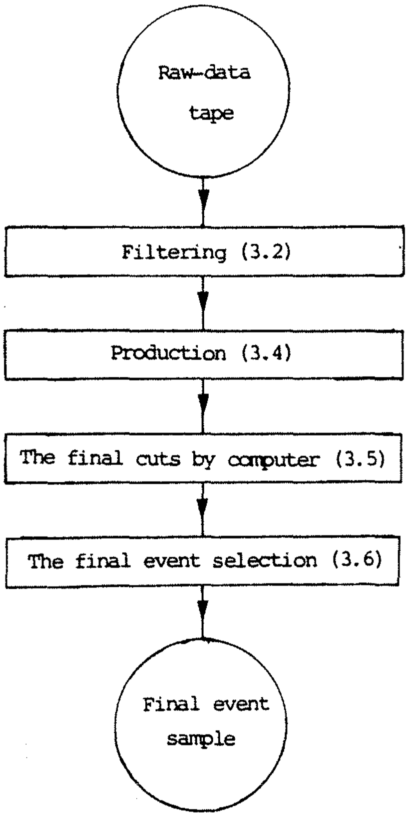

Figure 23: The analysis chain.

3.2 FILTERING

All events that passed the trigger were written to tape. To speed up the analysis (and decrease computer expenses) the data were first filtered with the following criteria:

a. Less then five hits in the veto system (for two – body final states).

b. Require more than 75 % of total lab – energy, E_{lab}, in the calorimeters (for many body final states).

$$E_{lab} = \sqrt{p_{\bar{p}}^2 + m^2} + m$$

$p_{\bar{p}}$ = beam momentum

m = proton/antiproton rest mass

For $p\bar{p} \rightarrow \chi_1 \rightarrow J/\psi\ \gamma \rightarrow e^+\ e^-\ \gamma$ only criterion b was used. The reason was that the γ might occasionally fire more than one veto due to overlap between the veto − counters, shower creation etc. This filter reduced the number of χ_1 triggers to be analysed from 623 673 to 165 286, a reduction of 74% .

3.3 THE OFFLINE ANALYSIS PROGRAM

Every trigger that passed the energy filter was analysed by the analysis program and those not fullfilling the criteria applied in the program were rejected. The program was written in FORTRAN and stored on a PAtchy Master file. PATCHY [39] is a system for handling large programs used by many users. Below a description is given of the offline analysis program. The parts which I have worked with will be described in detail while the interested reader is invited to study [41] for details of the other parts.

The flowchart of the MAIN program for the R704 offline analysis is given in fig. 24 .
The essential part of the program for the analysis is the routine ANALYS. There each event is analysed and various counters for the final run statistics are updated.

3.3.1 The routine ANALYS

As mentioned previously, the routine ANALYS is the nucleus in the offline analysis. It is called for each new file , see fig. 24, and inside it the relevant routines are called for each event. The original flowchart of ANALYS as given on the PAM − file [41] is given in fig. 25 .

The detector in the R704 experiment gave two independent ways of reconstructing tracks, namely by using the information from the analog chambers or the information from the MWPC's. Thus it was possible to have two separate ways of trackfinding. If the analog part failed, the MWPC's might work and the other way around. On the original PAM − file [41] these two different ways of trackfinding were not separated,thus lowering the efficiency of the analysis. To improve on this the order of calling

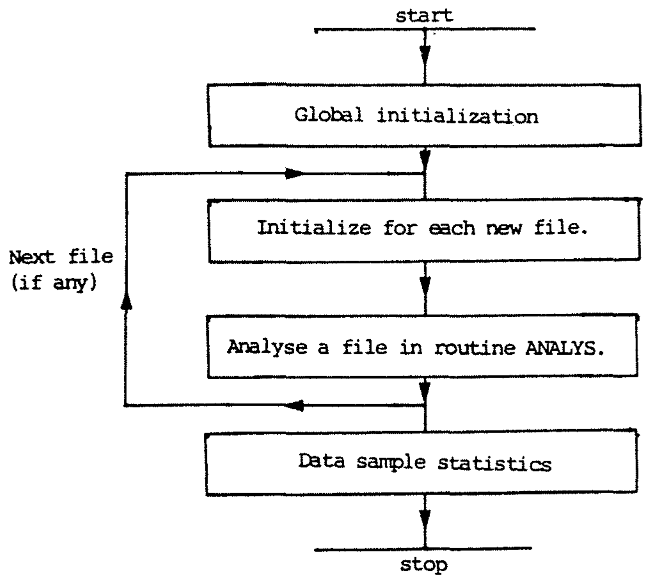

Figure 24: The flowchart of the MAIN program for the offline analysis in R704.

the routines in ANALYS were changed and some new routines (MYFOLL and DIGFOL) were added. The new version of the flowchart for ANALYS is given fig. 26. It gave two independent ways of finding events. That is, triggers that passed either the analog or the MWPC part or both were accepted. A higher efficiency of the analysis was thus obtained.

3.3.1.1 Track reconstruction

The routines (CLRNRM ,CODKLS and PATREC) for calculating the line parameters x, y, dx/dz, dy/dz from the MWPC information were already on the PAM−file. A description of them may be found in [41] or [31] and will not be repeated here. For the analog chamber some work was still to be done. Routines (MULTR, ACPR1 and ANCOR1) originally written at CERN were modified to suit the purposes of the Oslo analysis. For associating tracks with clusters in the precalorimeter and the lead glass, two new routines were written. MYFOLL for the analog chamber lines and DIGFOL for the MWPC lines.

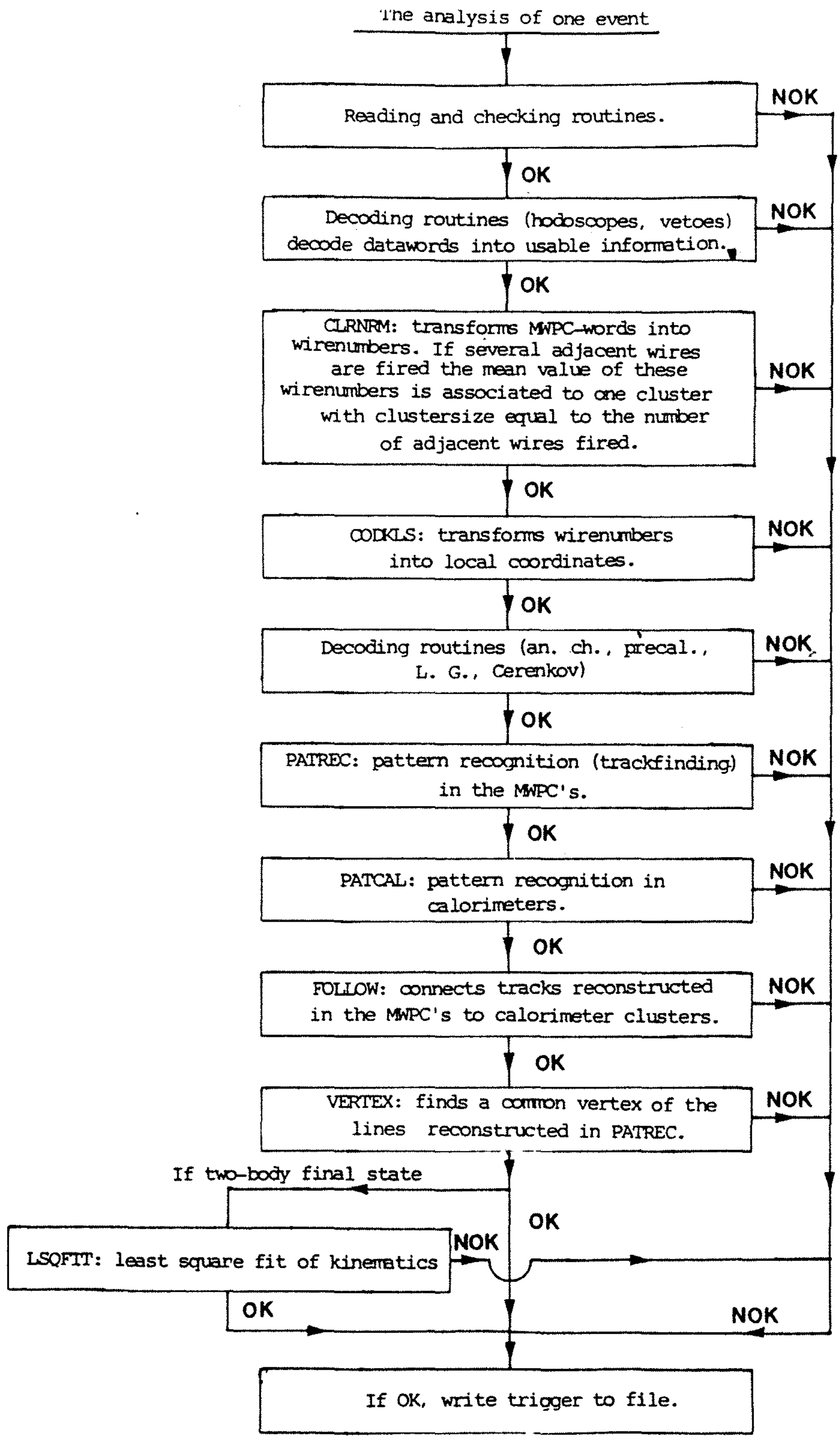

Figure 25: The flowchart of ANALYS, original version.

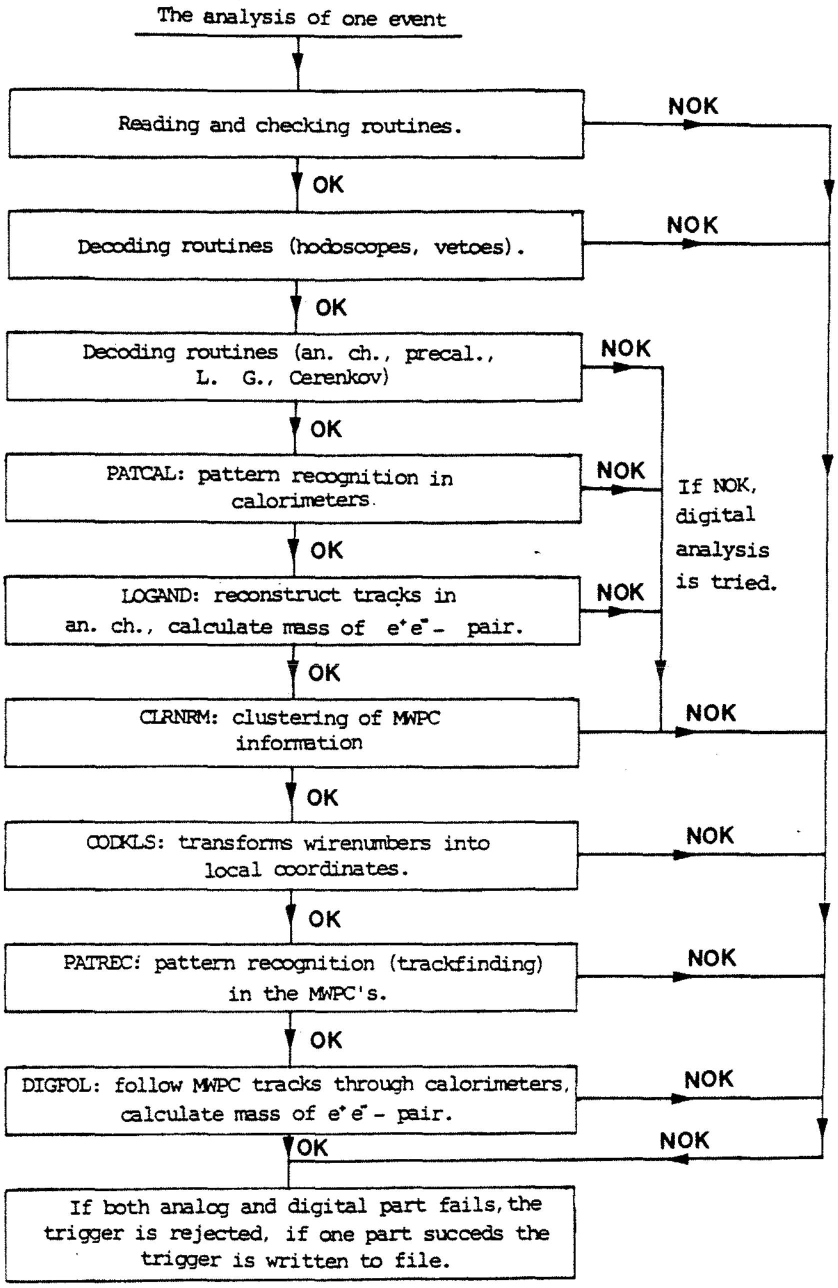

Figure 26: The flowchart of ANALYS, improved version.

The track reconstruction in the analog chambers was done in the routine LOGAND. Its lay−out is shown in fig 27.

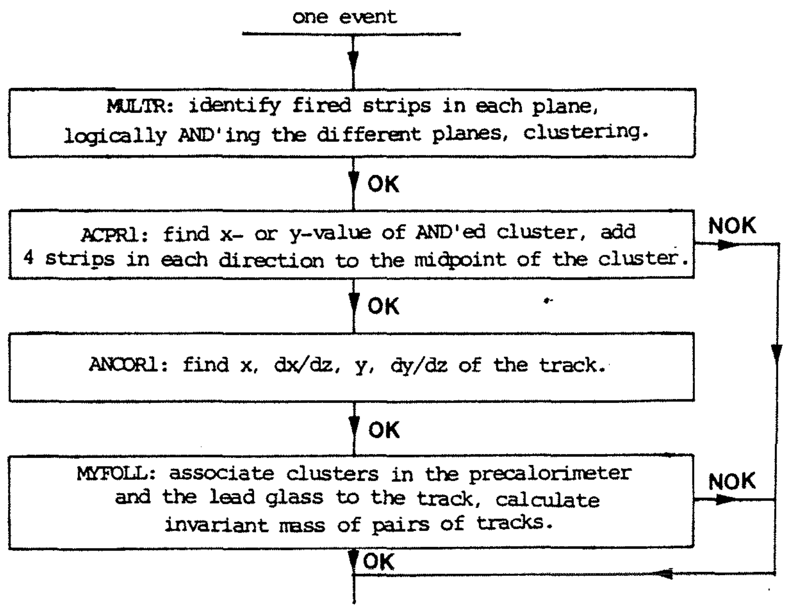

Figure 27: Flowchart of the routine LOGAND.

3.3.1.2 The routine MULTR

In the routine MULTR three tasks were performed

i. An array MPATI was set according to which strips were fired in the analog chambers. This information was fetched from the array ADCCA2(IPLANE,ISTRIP,IARM), which contained the signal in plane IPLANE, strip ISTRIP and arm IARM. MPATI(KK,NAC,NVIEW) has three indexes:

KK = 1,4 = word number

NAC = 1,4 = chamber number

NVIEW = 1,4 = x or y plane arm 1 or arm 2

Each word in MPATI holds information from 32 strips of the analog chambers. There were 108 strips in the x−direction and 96 in the y−direction, so 4 words were needed to describe one plane of strips (for the y−direction 3words are enough, but to simplify the algorithm 4 were used). One word consisted of 32 bits (IBM). A fired strip and its adjacent strips, to take into account tracks with large incident angles, were given the value 1, while the remainig strips were assigned the value 0. The routine SBIT1(MPATI(KK,NAC,NVIEW),KKK) was used to assign the number 1 to bit number KKK in word KK, chamber NAC and plane NVIEW for each fired strip and its adjacent. An example of how a word in MPATI looked is given below.

ii. Using the FORTRAN logical AND−operation the different planes were compared with each other. This in order to get a line through the analog chambers. In each arm there were 8 planes, 4 x−planes and 4 y−planes. The 4 x−planes were compared with each other in the following way:

```
            MPAT(KK,NVIEW) = MPATI(KK,1,NVIEW)
            DO 11 NAC=2,4
   11       MPAT(KK,NVIEW)=AND(MPAT(KK,NVIEW),MPATI(KK,NAC,NVIEW))
```

Here the first x−plane is compared with x−plane 2 and if the same bit is assigned the value 1 in both planes the same bit is assigned the value 1 in MPAT as shown below:

MPATI, x−plane 1, first word	000000011111000000011011100011100
MPATI, x−plane 2, first word	00000010111110000000111111100011000
AND−operation	
MPAT, x−planes, first word	00000000111100000001101110001 1000

This AND−ed MPAT of plane 1 and 2 is then AND−ed with plane three and the MPAT resulting from that operation is AND−ed with the fourth and last plane. The final version of MPAT will contain information of which strips that were fired in all the four x−planes. The same process is applied to the y−planes.

iii. To get some more usable information out of MPAT, adjacent fired strips were connected in clusters. The information in the array MPAT was searched for clusters and filled into the array MRESUL:

MRESUL(1,IKL(I),I): contained the first stripnumber in the cluster

MRESUL(2,IKL(I),I): contained the clustersize

I refers to the AND'ed x− or y−plane arm 1 and 2 and IKL(I) is cluster number IKL in plane I. Maximum 5 clusters (tracks) were allowed in each x− or y−projection. Inside each cluster up to 3 empty strips were accepted to allow for ineffectivities. E.g. the sequence

0011 1100 1100 0000

would be recognised as one cluster.

3.3.1.3 The routine ACPR1

The array MRESUL from the routine MULTR contains the information of each of the AND'ed planes. E.g. information from each of the 4 x−planes arm 1 have been compared in the AND−operation, and the result stored in the elements MRESUL(1,IKL(I),I) and MRESUL(2,IKL(I),I). The x′−value of each cluster is found by

$$x' = \text{MRESUL}(1,\text{IKL}(I),I) - 1 + \text{MRESUL}(2,\text{IKL}(I),I)/2.$$

the -1 term being due to the way of counting, see fig. 28.

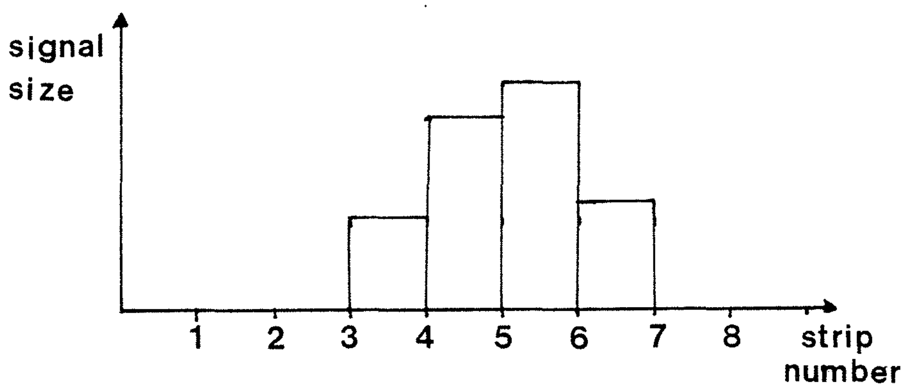

Figure 28: Example of signal in an analog chamber.

This x'-coordinate was then transformed to the different x-planes using:

$$x = x' \, z/z_{media}$$

where

$$z_{media} = (z_{plane3} + z_{plane5})/2$$

and z is the z-coordinate of plane x. It is assumed that the vertex is at origo. This x-value was transformed into the strip number N, defining the midpoint of the AND'ed cluster in the x-plane. To this midpoint 4 strips were added in each direction to give the strips to be summed over when the x- (and y-) values of the different tracks should be found in the routine ANCOR1. The number of strips to be added in each direction, 4 , was the value found to give best hadron/electron separation [40]. The mean cluster size in the analog chambers was $\cong 4$.

3.3.1.4 The routine ANCOR1

In this routine the line parameters x, y, dx/dz and dy/dz of the track were found. This was done in two steps:

i. First the x− and y−values of the different planes were found. The center of gravity of the cluster was calculated

$$x_{cog} = \Sigma\ (i-0.5)\ q_i\ /\Sigma\ q_i$$

where the sums are over i and i run from the first strip in the cluster to the last one, that is the midpoint strip found in the routine ACPR1 ± 4 strips. q_i is the signal in strip i, pedestal subtracted. The factor $(1-0.5)$ arise from the fact that the signal should be assigned to the middle of the strip, not to the side of it.

ii. After the first step each plane has its x− or y−value. That is in each arm there are 4 x_{cog}−values and 4 y_{cog}−values. These 4 x_{cog}−values are then used to make a fit to a line:

$$x_i = a\ z_i + b$$

where i runs over the four planes and z_i is the known z−position of x−plane number i. The small distance $z_4 - z_1 \cong 6$ cm compared with $z_{media} \cong 120$ cm implies that a small error in x_{cog} leads to a big error in the slope estimate a = dx/dz. Therefore the slope was estimated using:

$$a = x_i/z_{media}$$

In addition to calculating the line parameters of a line, the energy deposited in the analog chamber and associated to the line were found:

$$Q = \Sigma\ q_{ik}$$

also calculate the width of the cluster

$$V_i = \Sigma\ q_{ik}\ [(k-0.5)-x_{cog}]^2/\Sigma\ q_{ik}\ ,\quad \text{sum over k}$$

and define a total width

$$V = 1/4 \Sigma V_i$$

were i runs over the four x−(y−) planes in one arm.

We now have a x−line characterised by the lineparameters x, dx/dz and an y−line with y, dy/dz. If two or more sets of x and y coordinates are obtained, the problem arises of associating x and y coordinates with a certain particle. To find which x− and y−line that should be associated and which precalorimeter− and lead glass−energy that should be associated to this combined (x,y)−line was the task of MYFOLL.

3.3.1.5 The routine MYFOLL

MYFOLL correlates x− and y−lines given from ANCOR1 and associates clusters in the precalorimeter and in the lead glass to the line. Finally it calculates the invariant mass for all combinations of pairs of correlated lines from arm 1 and arm 2, and cuts on the mass are performed. It works as follows:

The input is x− and y−line parameters from ANCOR1. Correlation of the x− and y−lines for each arm:

Loop over all x−lines:

i. Predict where the x−line hits in the precalorimeter and the lead glass. This is done by a transformation of the x−value of the cluster at z_{anch} in the analog chamber to the x−value of the cluster in the precalorimeter at z_{precal} or the lead glass at z_{LG}.

ii. Loop over all y−lines. Predict where the y−line hits in the precalorimeter and the lead glass.

iii. Loop over all $\theta-$ and $\phi-$clusters in the precalorimeter and all the lead glass clusters. Calculate the distance between the predicted hit of the line and the measured c.o.g. of the cluster. The c.o.g. of the precalorimeter and the lead glass clusters are calculated in the routine PATCAL. If these distances, called RPR for the precalorimeter (RPR = x_{pred}(precal) $-$ x_{cog}(precal)) and RLG for the lead glass, are less than RPRCUT and RLGCUT, the clusters are correlated to the line. The values of RPRCUT and RLGCUT were tuned in by running the program on the already analysed J/ψ events. The values thus obtained are given in fig. 29 .

If no correlated lines were found in an arm, the trigger got no analog analysis.

We now have correlated $x-$ and $y-$lines in both arms. The next step is to calculate the invariant mass, the J/ψ mass in the process $\chi_1 \rightarrow J/\psi\,\gamma \rightarrow e^+\,e^-\,\gamma$, for all combinations of pairs of correlated lines in arm 1 and arm 2. This was done using:

$$p_1 = (E_1, \vec{p_1}) \quad \text{, four momentum electron 1, lab}$$

$$p_2 = (E_2, \vec{p_2})$$

$$p_{J/\psi} = (m_{e^+e^-}, \vec{0}) \quad \text{, four momentum } J/\psi \text{ in CMS}$$

Using Lorentz invariant four momentum conservation

$$m_{e^+e^-}{}^2 = (E_1 + E_2)^2 - (\vec{p_1} + \vec{p_2})^2$$

having highly relativistic electrons we assume $m_e \approx 0$ and get

$$m_{e^+e^-}{}^2 = 2\,E_1\,E_2\,(1 - \cos\theta)$$

$\cos\theta$ being the angle between $\vec{p_1}$ and $\vec{p_2}$.

The angle θ between the two lines in arm 1 and arm 2 was needed. It was calculated in the following way. For each line i a unit vector $\vec{e}$ was defined:

$$a = dx/dz$$

$$b = dy/dz$$

$$c = dz/dz = 1$$

$$\det = \sqrt{a^2 + b^2 + 1}$$

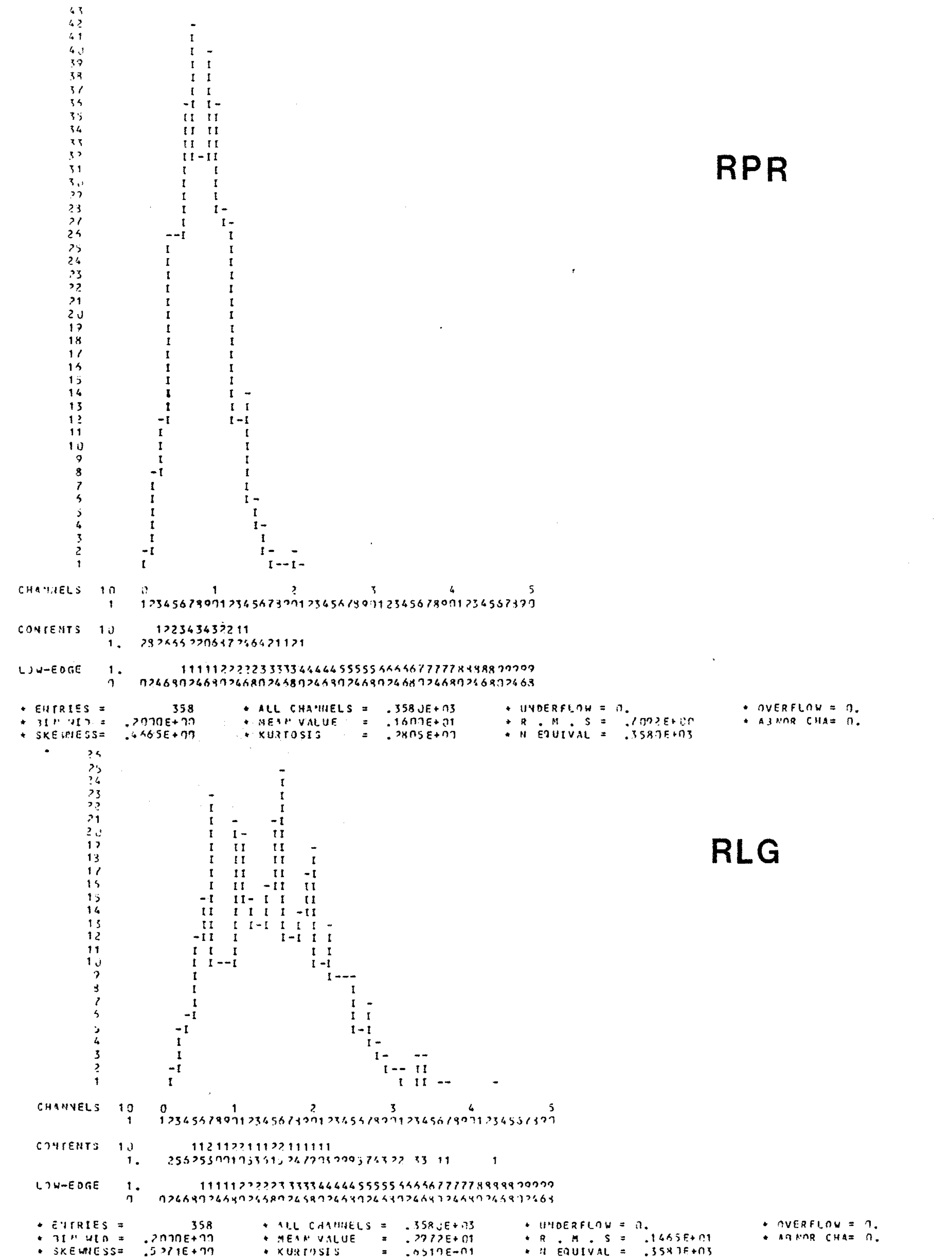

Figure 29: RPR and RLG for MYFOLL, J/ψ.

$$\vec{e}_i = (a/det,\ b/det,\ 1/det)$$

Taking the dot product between two unit vectors, $\cos\theta$ is found.

$$\cos\theta = \vec{e}_i \cdot \vec{e}_j$$

The energies E_1 and E_2 of the incident electron/positron were mainly deposited in the precalorimeter and in the lead glass and calculated as follows:

i. In the precalorimeter the variable ENECA2 contains the energy of the cluster, pedestal subtracted and normalised to m.i.p. (minimum ionizing particles). The energy in GeV was then found by

$$E_{precal} = \mathrm{ENECA2} \cdot \mathrm{CALPR}$$

where CALPR is a calibration constant.

ii. The procedure was similar for the lead glass, but the calibration constants CALLG were energy dependent and so an iterative procedure was used.

$$E_0 = \mathrm{ENECA3} \cdot (\mathrm{CALLG}_1 + \mathrm{CALLG}_2)$$

$$E = \mathrm{ENECA3} \cdot (\mathrm{CALLG}_1 + E_0 \cdot \mathrm{CALLG}_2)$$

E_0 being the first approximation and E the final energy deposited in the lead glass in GeV. ENECA3 is the signal normalised to m.i.p. and pedestal subtracted, and $\mathrm{CALLG}_{1,2}$ are calibration constants.

Having all information the invariant mass of the two lines could be calculated. If there was more than one pair of lines, the information about the pair which had the highest invariant mass was stored, if the mass was above the cut applied.

3.3.1.6 The routine DIGFOL

For the digital part of the analysis the line parameters were found in the routine PATREC. Since the MWPC's had three planes X, Y and U with different wire orientations, see fig. 14 , there were no problems of associating x− and y−lines. So the task of DIGFOL was to assign clusters in the precalorimeter and the lead glass to the MWPC line. It worked as follows:

i. Predict where in the precalorimeter and the lead glass the line hits.

ii. Loop over all $\theta-$ and $\phi-$clusters in the precalorimeter and all the lead glass clusters. Calculate the distance between the predicted hit of the line and the c.o.g. of the clusters. If these distances, RPR and RLG, are less than RPRCUT and RLGCUT, the clusters are assigned to the line.

Then the invariant mass of the two lines were calculated in the same way as in MYFOLL. The values for RPRCUT and RLGCUT for the MWPC's were slightly different from those used in the analog part of the analysis, see fig. 30 .

3.3.1.7 The uncertainty in the mass calculations

Below we estimate the uncertainty in the calculations of the invariant mass $m_{e^+e^-}$:

$$\sigma_{m^2_{e^+e^-}}/m^2_{e^+e^-} = \sqrt{(\sigma_{E_1}/E_1)^2 + (\sigma_{E_2}/E_2)^2 + (\sigma_{\cos\theta}/[1 - \cos\theta])^2}$$

We have

$$(\Delta E/E)_{FWHM} = 0.28/\sqrt{E}$$

For a Gaussian ditribution the FWHM is related to the standard deviation through:

$$FWHM = 2\sqrt{(-2\log[1/2])}\,\sigma = 2.3548\,\sigma$$

giving

$$\sigma_{E_i}/E_i = (1/2.3548)\ 0.28/\sqrt{E_i}$$

The greatest value of $\cos\theta$ is $\cong 0.7$ giving $(1-\cos\theta) \cong 0.3$. We know that $\sigma_\theta \cong 3-4$ mrad which gives $\sigma_{\cos\theta} \sim 10^{-3}$, thus we ignore the contribution from $\sigma_{\cos\theta}/(1-\cos\theta)$. Taking typical values for the energy deposited in each arm, $E_1 = E_2 = 2.55$ GeV gives:

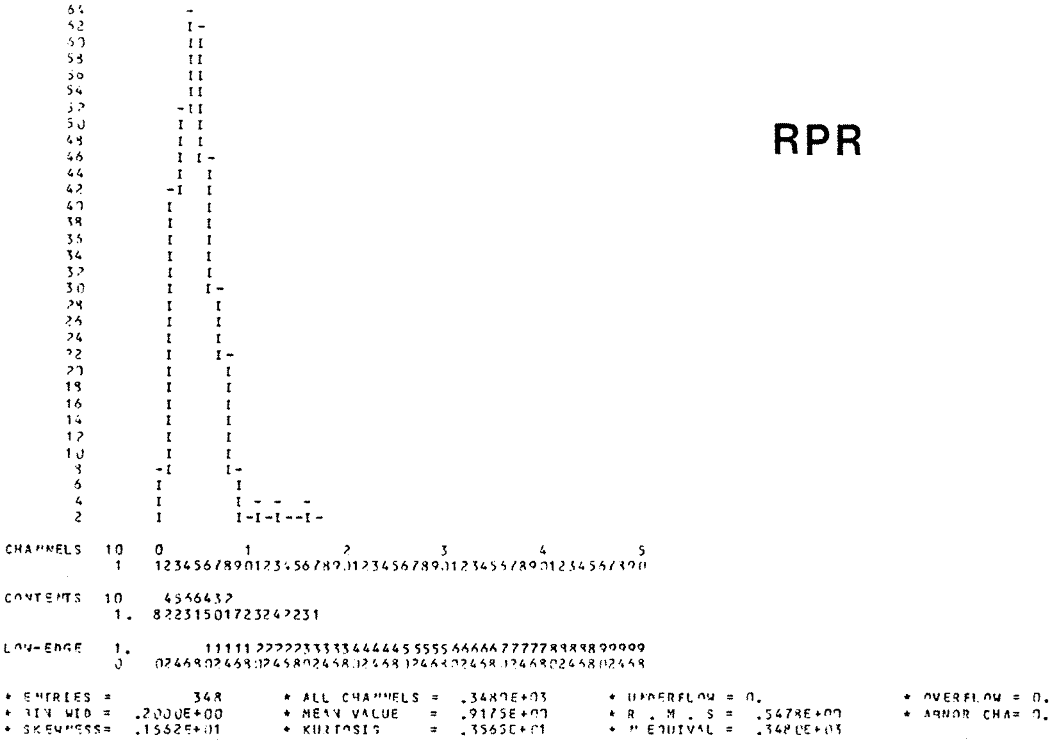

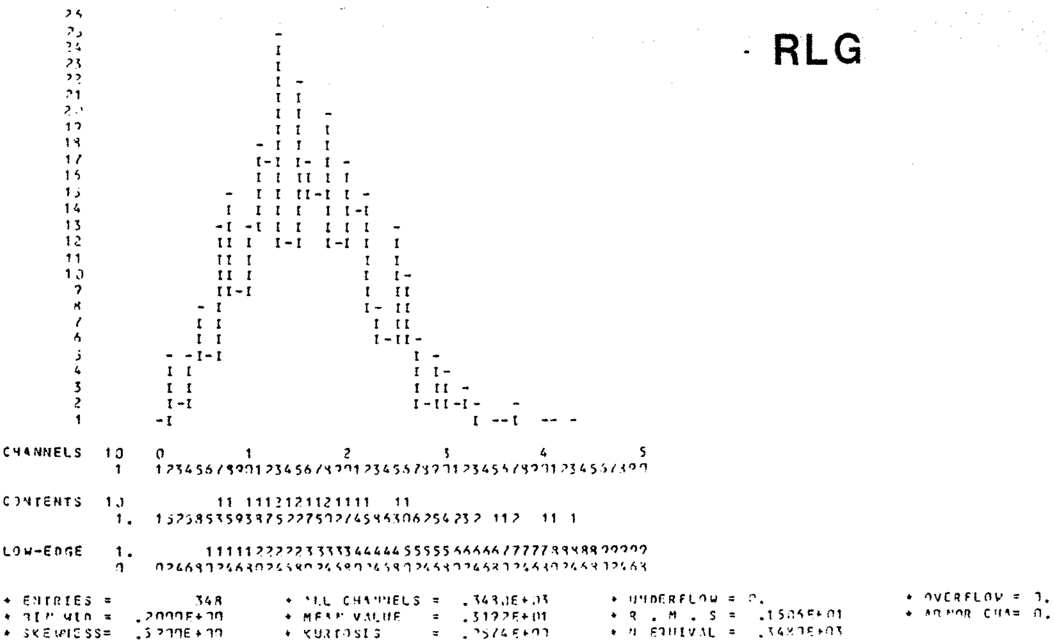

Figure 30: RPR and RLG for DIGFOL, J/ψ.

$$\sigma_{m^2_{e^+e^-}}/m^2_{e^+e^-} \cong 0.11$$

and

$$\sigma_{m_{e^+e^-}}/m_{e^+e^-} = 1/2\, \sigma_{m^2_{e^+e^-}}/m^2_{e^+e^-} = 0.06$$

That is an uncertainty in the mass calculations of 6 %.

3.4 PRODUCTION

A total of 165 286 χ_1 triggers passed the filtering process. The next step was the production. Using the program described in the previous section requiring $m_{e^+e^-} > 2.4$ GeV and using very loose values for RPRCUT = 10 cm and RLGCUT = 15 cm both in DIGFOL and MYFOLL, the number of triggers that passed the production was 1598. It should be mentioned that the total number of fired vetoes were required to be less than 15. This was due to computer problems. Also a filter (CHIFLT) was used to speed up the digital part of the analysis. Triggers with two or more clusters in at least two of the MWPC planes in at least one of the two small chambers were rejected in the MWPC analysis. This filter speeded up the analysis by a factor 5.

All the J/ψ events passed the production program when tested on it. Out of 1598 triggers which passed the production, 1478 passed the analog part of the analysis and 374 passed the digital part. This discrepancy had mainly two reasons:

i. To speed up the digital analysis, a filter, CHIFLT, was used.

ii. There was no quality control of showers in the analog chambers.

To summarise, by using very mild simple cuts only 1598 ($\approx$ 1 %) triggers out of 165 286 passed the production stage. This reduction clearly shows the strength of the R704 experiment in detecting electron positron pairs. The information from the production – runs are given in table 4.

The same program was used on the $^1P_1$ production. Results from that analysis is given in appendix D.

Table 4: Information from the production, χ_1.

Run number *** *** ***	Total number passing ***	Number of triggers to be analysed	Computer time used sec)* ***	Triggers passing analog part	Triggers passing digital part	Triggers passing digital part only
1090 – 1096	138	14 457	6620.101	128	36	10
1097 – 1101	171	18 330	8499.040	160	40	11
1102 – 1106	106	10 776	5437.646	97	23	9
1107 – 1112	160	15 747	7280.525	144	47	16
1113 – 1117	80	6 969	3399.349	73	18	7
1118 – 1121	94	11 004	5218.290	88	23	6
1122 – 1128	144	14 803	6875.532	127	31	17
1129 – 1135	194	19 009	8823.643	175	45	19
1136 – 1141	118	14 608	5971.639	111	22	7
1142 – 1144	70	9 222	4537.110	65	17	5
1145	23	3 120	1471.922	19	5	4
1146	38	3 246	1444.676	37	4	1
1148**	38	2 567	1286.380	35	12	3
1149	34	2 374	1062.018	34	4	0
1150	30	2 570	1313.651	30	6	0
1151 – 1158	160	16 484	8386.916	155	41	5
Total	1598	165 286	77628.438	1478	374	120

* CDC CYBER(170/835) CPU – sec.
** The observant reader may wonder where run 1147 is,well it never existed.

3.5 THE LAST CUTS BY COMPUTER

After the production the more tedious process of adjusting cuts for the final χ_1 event selection began. The already analysed J/ψ events were used as a bank of events for testing of cuts and finding the efficiency of the analysis.

The different cuts applied and the reason behind them are given below in the order in which they were applied.

3.5.1 Cut a C_i (Cerenkov) and S_i (S hodoscope) response

C_i is the Cerenkov response in number of photoelectrons. One incident electron gave on the average 5.5 photoelectrons [29]. The Cerenkov might be fired by electrons coming from the process $\gamma \rightarrow e^+e^-$ where the γ converts into electrons either in the beampipe,the S_i hodoscope or in the Cerenkov entrance (the photon comes from e.g. π^0). The two electrons will on the average give a higher number of photoelectrons than the single electron expected in one arm in the process $\chi_1 \rightarrow J/\psi\gamma \rightarrow e^+e^-\gamma$. Thus restrictions may be put on the C_i signal.

S_i is the number of m.i.p.'s in the S hodoscopes in arm 1 or arm 2. The mean value of S_i for an incident minimum ionizing particle is $\cong$ 1. A value of $S_i \cong 2-3$ m.i.p. may be consistent with $\pi^0 \rightarrow \gamma\gamma$ where the γ converts to $\gamma \rightarrow e^+ e^-$ and the π^0 is produced in the process $p\bar{p} \rightarrow \pi^0$ + anything.

A combined S and C cut was used. Triggers with $S_1 > 2.2$ m.i.p. and $C_1 > 8.7$ p.e. or $S_2 > 1{,}9$ m.i.p. and $C_2 > 10$ p.e. were rejected. The cut values were obtained from J/ψ data, see fig. 31. .

1022 out of 1598 χ_1 triggers passed this cut.

3.5.2 Cut b $S_1 + S_2$

The combination $S_1 + S_2$ was required to be less than or equal to 4.4 m.i.p.. One of the electrons was thus allowed to be on the tail of the signal distribution in the S hodoscopes.

806 out of 1022 χ_1 triggers passed this cut.

3.5.3 Cut c Vertex−parameter

The vertex−parameter was defined to be the shortest distance between two lines, one from each arm.

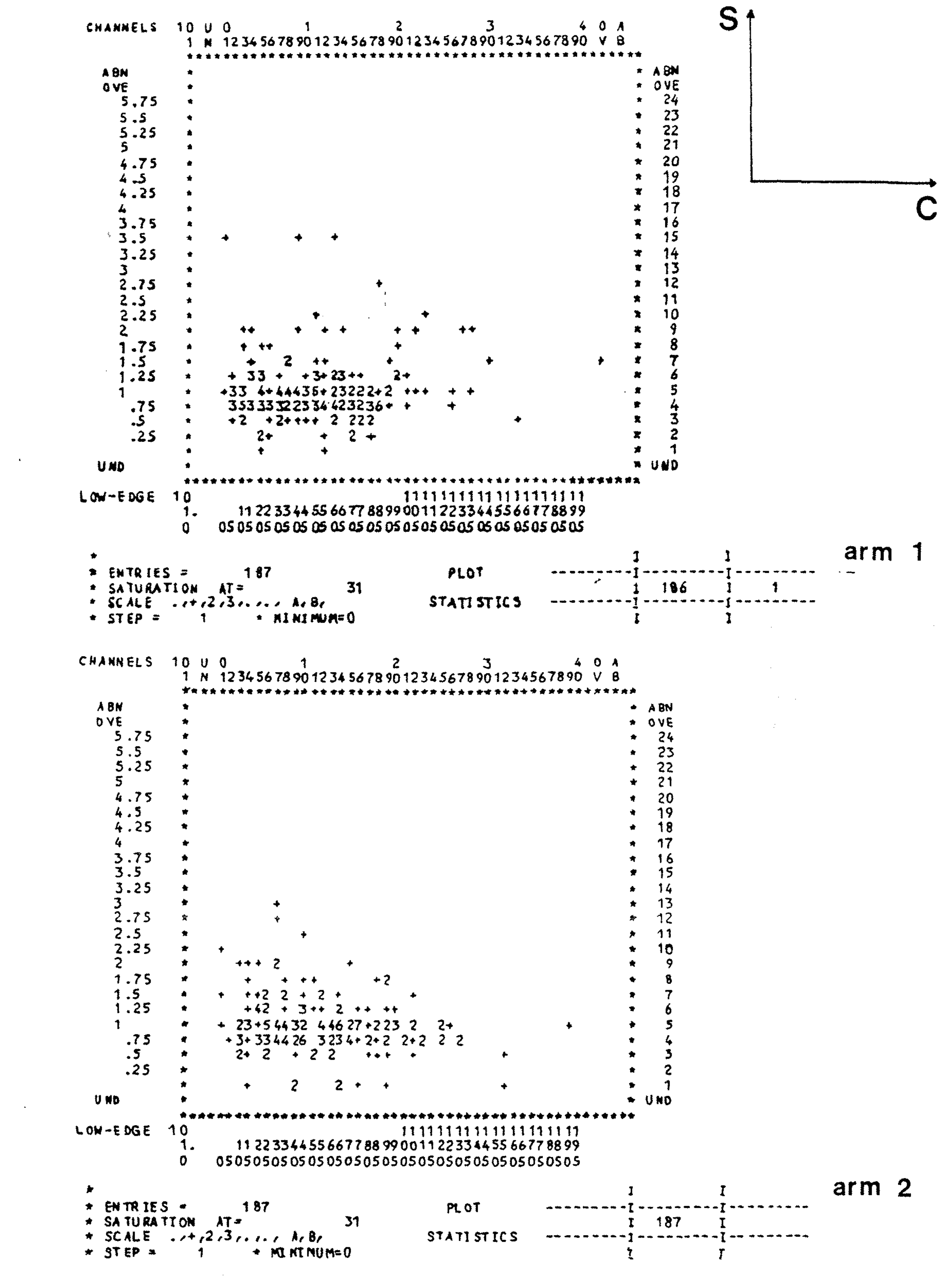

Figure 31: The C and S distribution for J/ψ, arm 1 and arm2.

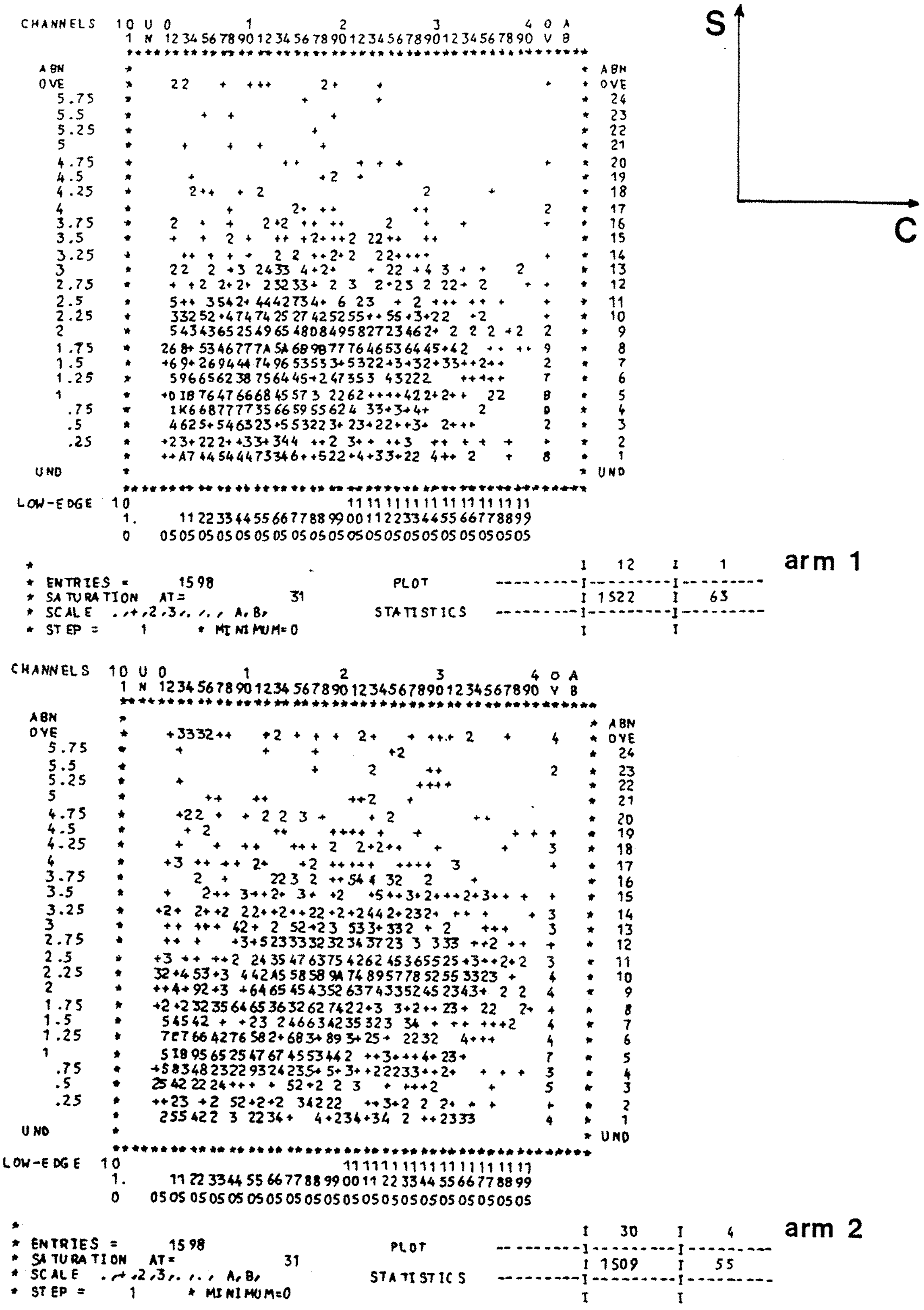

Figure 32: The C and S distribution for 1598 χ_1 triggers, before cut a.

Let x_1, y_1, z_1 be the coordinates of the impact point in arm 1 in the reference system. The line going through this point is described by the unit vector $\vec{e_1}$. For arm 2 we have x_2, y_2, z_2 and $\vec{e_2}$. The shortest distance r between the two lines is:

$$r = \vec{k} \cdot \vec{d} / |\vec{k}| \quad \text{(in cm)}$$

$$\vec{k} = \vec{e_1} \times \vec{e_2}$$

$$\vec{d} = (x_2 - x_1, y_2 - y_1, z_2 - z_1)$$

Using the bank of J/ψ events r was required to be less then 1.2 cm (fig. 33). While applying this cut, CHIFLT was not active. This because the vertex−parameter cut was only used on the MWPC part of the analysis, and to increase the number of MWPC candidates, CHIFLT was deactivated.

784 out of 801 χ_1 triggers passed this cut.

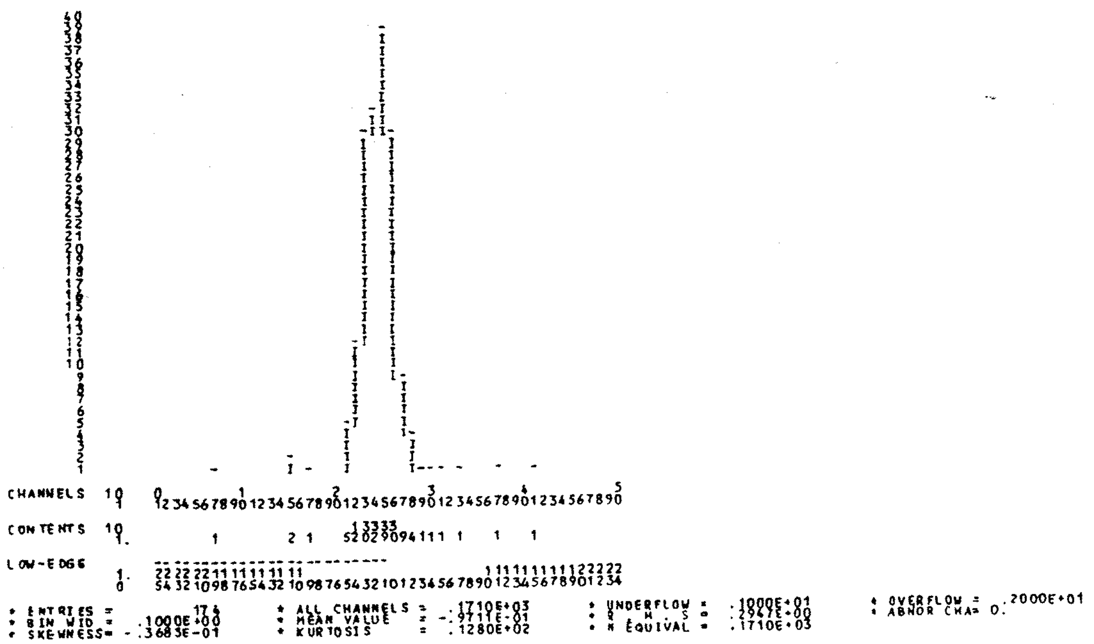

Figure 33: The vertexparameter distribution for the J/ψ.

3.5.4 Cut d Extra clusters in the precalorimeter.

A χ_1 event should give one main cluster in the precalorimeter in each arm due to the electrons and maybe an additional cluster caused by the γ. Thus it was possible to reject events that had more than one 'major' extra cluster in one arm. To define a 'major' extra cluster the J/ψ event bank was used. Some J/ψ events had minor extra clusters close to the main cluster. To maintain a high J/ψ efficiency these minor extra clusters were allowed in the χ_1 analysis. The definition of a 'major' extra cluster was different for the $\theta-$ and the $\phi-$planes in arm 1 and arm 2 and are given in table 5 .

Table 5: Definition of 'Major' extra cluster

'Major' extra cluster	Distance from used cluster (cm)	Energy deposited (m.i.p.)
θ_1	$\geq$ 5.2	$\geq$ 3.4
ϕ_1	$\geq$ 4.2	$\geq$ 1.0
θ_2	$\geq$ 7.2	$\geq$ 0.8
ϕ_2	$\geq$ 5.0	$\geq$ 2.0

425 out of 784 χ_1 triggers passed this stage.

3.5.5 Cut e Cut sharpening

The only two cuts used in the production were sharpened.

i. The invariant mass of the two lines was required to be $\geq$ 2.6 GeV.

ii. RPRCUT and RLGCUT were optimized:

For MYFOLL	RPRCUT = 4.2	RLGCUT = 8.6
For DIGFOL	RPRCUT = 3.4	RLGCUT = 8.6

187 out of 425 χ_1 triggers passed i.

149 out of 187 χ_1 triggers passed ii.

3.5.6 Cut f Veto cut

In the process $\chi_1 \rightarrow J/\psi\ \gamma \rightarrow e^+\ e^-\ \gamma$ one should expect never to have more than one neutral veto fired. However reality is not that simple. The veto−counters overlap to some extent and the γ may give rise to showers that may fire both charged and neutral vetoes. Even so it is possible to set an upper limit on the number of fired vetoes. In the J/ψ data maximum 2 charged vetoes were fired, maximum 1 neutral veto fired and maximum 2 totally fired for any event. With this in mind and allowing for the single γ the following upper limits were set:

Not more than 4 charged vetoes fired.

Not more than 4 neutral vetoes fired.

124 out of 149 χ_1 triggers passed this cut.

3.5.7 Cut g Shower quality in the analog chambers

As previously noted, more triggers passed the analog than the digital part of the analysis. To further reject background passing the analog part additional cuts involving only the analog part were introduced. The width V and the energy Q of the analog chamber track were known, see 3.3.1.4. Using the J/ψ bank as a test sample, lower limits on V and Q were set. A track with a small Q and a small V has a small probability of being a shower, but is rather an indication of a single minimum ionizing particle. In the analog chambers the incident electrons should have converted into a shower. The limits on Q and V were

$$Q > Q_{cut} = 100 \text{ ADC channels}$$

$$V > V_{cut} = 5000$$

Out of the 124 χ_1 triggers passing cut a−f, 122 passed the analog part. Of these 122 analog triggers 95 passed cut g. In total a number of 101 triggers were left to be scanned visually and that scan is described in the next section.

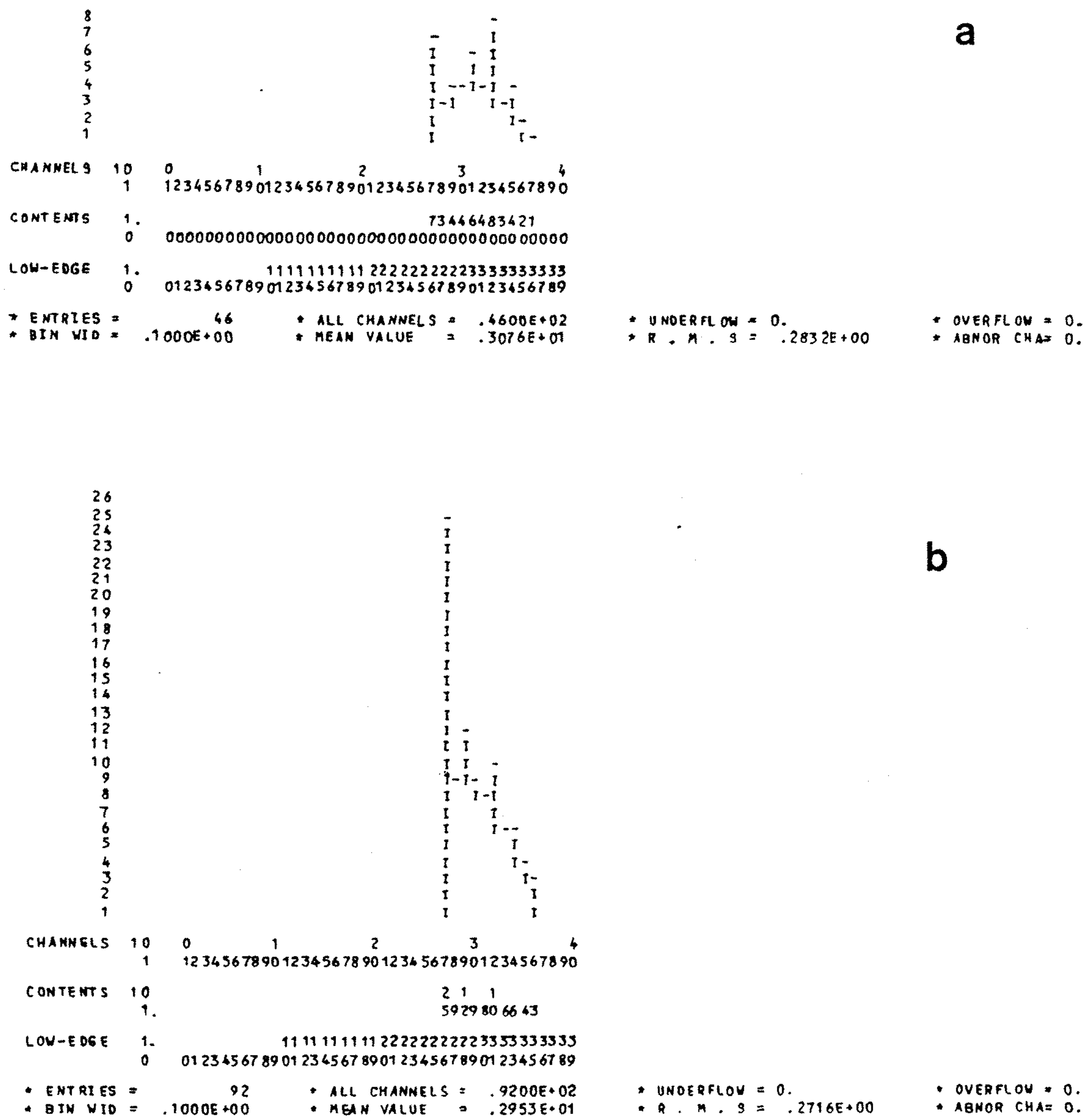

Figure 34: The mass distribution of 101 χ_1 triggers.
a. Triggers which passed the digital part.
b. Triggers which passed the analog part.

3.6 THE FINAL EVENT SAMPLE

The final event selection was done by a visual scan. The information from each of the 101 χ_1 triggers left was studied in detail. Together with constraints from the kinematics of the process $\chi_1 \rightarrow J/\psi\ \gamma \rightarrow e^+\ e^-\ \gamma$ all candidates that showed some weakness were removed.

i. The kinematics of the process $\chi_1 \rightarrow J/\psi\ \gamma \rightarrow e^+\ e^-\ \gamma$ was calculated by a routine called CHIDEC. From the knowledge of the directions of the electrons, assuming relativistic electrons ($m_e = 0$), the electron momenta, the photon direction and momentum can be found (see appendix B for this calculation). The calculated photon direction was used to predict where in the detector a signal should have been seen. This information gave the following requirements:

- If there was an extra cluster greater than 1.5 m.i.p. in the precalorimeter it should be γ compatible, and no big ADC signal should be observed in neutral vetoes.
- If the γ was predicted in the veto system, it should be found in the predicted veto−counter within the accuracy of the prediction (for the accuracy of CHIDEC see appendix B).

ii. In the precalorimeter the electrons should have converted into a shower and a signal of several m.i.p.'s should be observed, on average 15 m.i.p. A much smaller signal may be consistent with pions, which is then a fake signal. Pions, $\pi^{\pm}$, may knock out electrons from the constituent atoms in the Cerenkov gas. These electrons ($\delta-$rays) can fire the Cerenkov, giving a fake trigger, while the pions are detected in the precalorimeter where they roughly give a signal ~ 1 m.i.p.. The $\theta-$ and $\phi-$clusters in the precalorimeter associated to the electron line were required to be greater then 1.5 m.i.p.

iii. The MWPC's are believed to be well behaving and well understood [29]. In the case when the MWPC's worked and PATREC found lines, but these lines were clearly missing the clusters in the precalorimeter and the lead glass, the trigger was rejected.

iv. The cuts on the S hodoscope signal S_i and the Cerenkov response C_i were thightened, requiring $S_i \leq 2.0$ m.i.p. and $C_i < 15.0$ p.e.

v. The analog chamber response was carefully studied, looking especially for double peaks coming from symmetrical π^0 decays. Triggers having double peaks in the analog chamber were rejected.

Out of the 101 χ_1 triggers before the visual scan, 31 passed the requirements i to v, see table 6. A list of these events are given in appendix E. Their mass distribution is shown in fig. 35 .

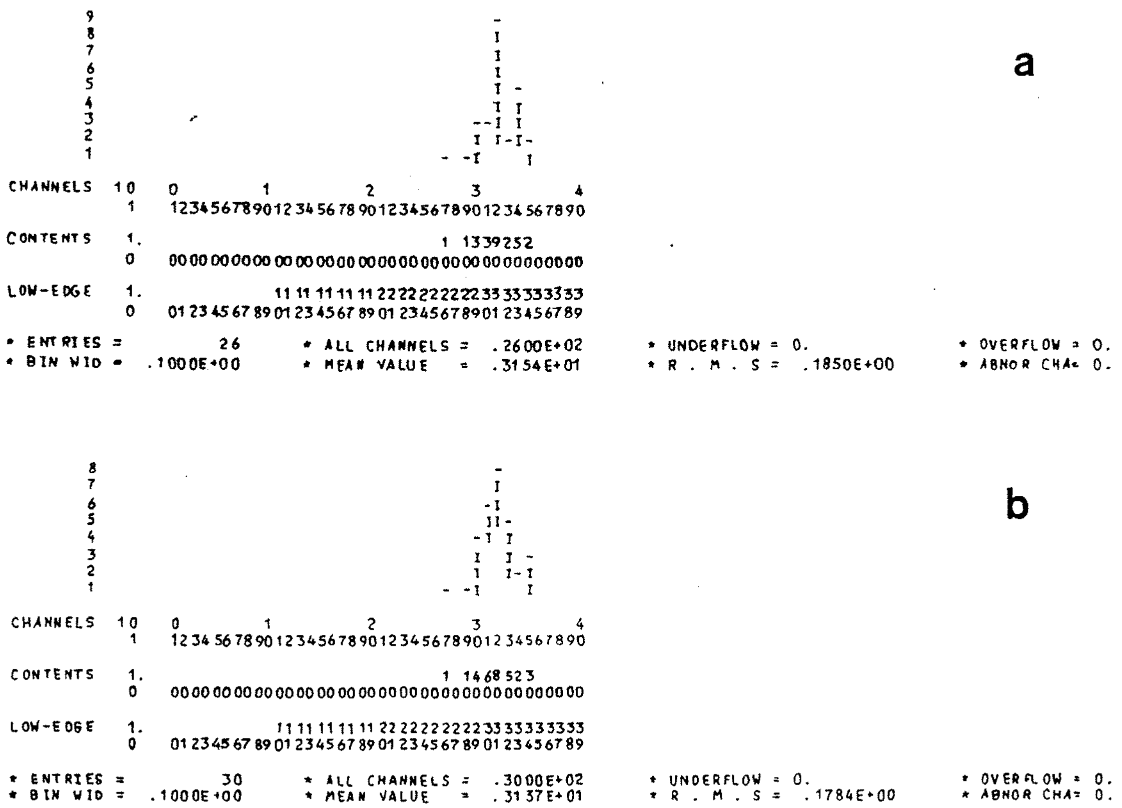

Figure 35: The mass distribution for the final χ_1 event sample.
a. Triggers passing the digital part.
b. Triggers passing the analog part.

Table 6: Rejection statistics for the final cuts, χ_1.

Cut	Number in	Number out
i	101	53
ii	53	45
iii	45	40
iv	40	34
v	34	31

3.7 SUMMARY

31 χ_1 triggers passed all cuts given in 3.4 – 3.6. A list over the different cuts and the number of triggers passing each stage is given below in table 7.

Table 7: Rejection statistics, χ_1.

Numbers of triggers started with ***	Cut *** *** ***	Number of triggers passing the analog part	Number of triggers passing the digital part	Number of triggers passing in total
623 673	Filtering	***	***	165 286
165 286	Production	1478	374	1 598
1 598	a	945	262	1 022
1022	b	743	236	806
806	c	743	198	784
784	d	400	136	425
425	e	145	50	149
149	f	122	46	124
124	g	92	46	101
101	Visual scan	30	26	31

Out of the 31 χ_1 events 5 were found to have the γ inside one of the two arms. In 21 cases the γ hit veto – counters and 5 γ's missed the detector in accordance with the predictions from CHIDEC. For the γ's which hit inside the arms, the energy deposited was measured and plotted against the one predicted from CHIDEC, see fig. 36 .

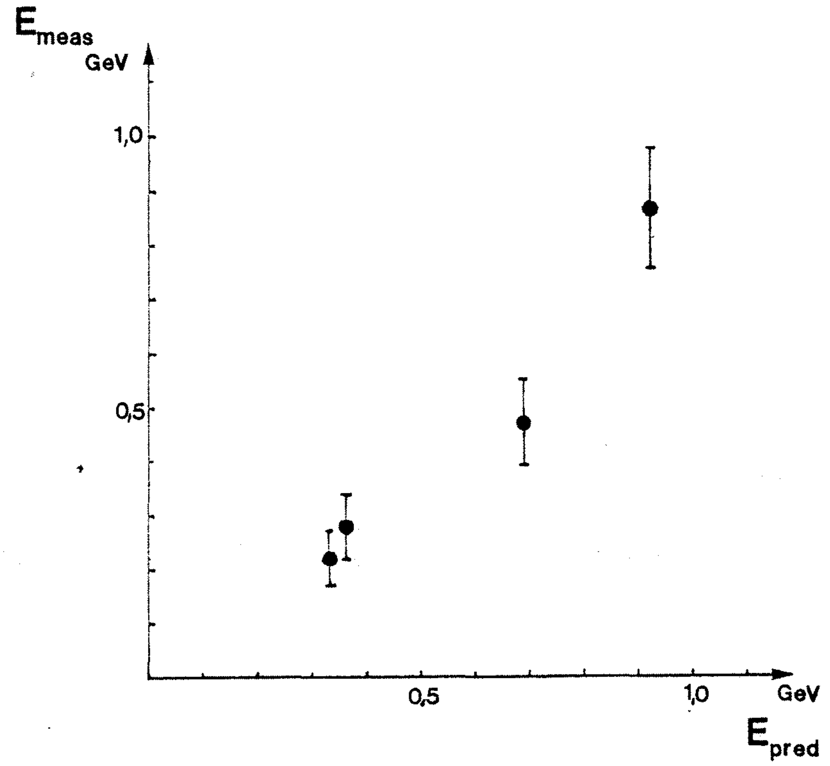

Figure 36: Measured towards calculated energy of the γ. Out of the 5 χ_1 with γ in one of the arms, one could not be used because the γ and the electron hit the same elements in the detector arm.

The background was estimated by applying the hole analysis chain to the data from the $^1P_1$ scan. 2 events passed the chain for an integrated luminosity $L^{^1P_1} = 1\ 019\ nb^{-1}$. The edges of the χ_1 scan were also included, being off resonance[10]. The background can then be given as:

[10] 'off resonance' was defined to be those bins where the expected number of events $\lambda_i < 0.1$, see chapter 4 for the definition of λ_i.

$$N_{bcg} = N_{pba}/(L^{^1P_1} + L_{\chi_1}^{off}) \times L_{\chi_1}^{on}$$

where

N_{bcg} = number of background events

N_{pba} = number of $^1P_1$ events passing the analysis chain

$L^{^1P_1}$ = integrated luminosity for the $^1P_1$ scan

$L_{\chi_1}^{off}$ = integrated luminosity for χ_1, 'off resonance'

$L_{\chi_1}^{on}$ = integrated luminosity for χ_1, 'on resonance'

inserting numbers, $N_{pba} = 2$, $L^{^1P_1} = 1019\ nb^{-1}$, $L_{\chi_1}^{off} = 90\ nb^{-1}$ and $L_{\chi_1}^{on} = 404\ nb^{-1}$ we get

$N_{bcg} = 0.7$ events

to be compared with the number of 31 χ_1 events that were found.

The efficiency of the analysis was estimated with the help of the J/ψ event bank. Out of 187 J/ψ's, 181 passed the computer cuts from a to g, giving an efficiency of 97 %. The total efficiency of the experiment for detecting the χ_1 state, will be discussed in chapter 4.

The analysis shows that R704 was succesful in detecting the electromagnetic decay channel of the χ_1 state. In chapter 4 the determination of the χ_1 parameters, m_{χ_1}, $Br(\chi_1 \rightarrow p\bar{p})$, $\gamma_{p\bar{p}}$ and Γ_{χ_1} will be discussed.

4. THE χ_1 PARAMETERS

4.1 INTRODUCTION

To determine the χ_1 parameters m_{χ_1}, the full width Γ, the branching ratio $Br(\chi_1 \rightarrow p\bar{p})$ and the partial width $\Gamma_{p\bar{p}}$ a maximum likelihood estimate was done. The detection efficiency was also included as a parameter in the fit.

4.2 THE METHOD

Given n independent observations the likelihood function L is defined as:

$$L(x_1,x_2,...,x_n|\theta_1,\theta_2,...,\theta_m)=f(x_1|\theta_1,\theta_2,...,\theta_m)\ f(x_2|\theta_1,\theta_2,...,\theta_m)...f(x_n|\theta_1,\theta_2,...,\theta_m)$$

where $f(x_i|\theta_1,\theta_2,...,\theta_m)$ is the probability density function and $\theta_1,\theta_2,...,\theta_m$ are unknown parameters. Thus L is the joint probability of the observation of x_i at fixed parameters θ_i. The best choice for the unknown parameters θ_i, according to the maximum likelihood principle, are those which maximise L. Hence we search solutions of

$$(\partial \ln L/\partial \theta_j)_{\theta_j=\hat{\theta}_j} = 0 \qquad j= 1, n$$

$\hat{\theta}_j$ being the parameters that maximise (minimise) ln L ($-$ln L). A sufficient requirement for having a maximum is:

$$(\partial^2 \ln L/\partial^2 \theta_j)_{\theta_j=\hat{\theta}_j} < 0$$

A detailed description of the maximum likelihood method may be found in [46].

4.2.1 THE LIKELIHOOD FUNCTION

If the integrated luminosity

$$\mathscr{L} = \int_{\Delta t_i} \mathscr{L}_i\,(t)\,dt$$

is known, the expected number of events, λ, can be calculated. $\mathscr{L}_i$ is the luminosity in the time interval Δt_i and assumed to be constant in Δt_i.

$\mathscr{L}_i\,(t) = \rho_i\, N_a\, N_{\bar{p}}\, N_{rev}$

ρ_i = jet density

N_a = Avogadros number

$N_{\bar{p}}$ = numbers of $\bar{p}$ in the ISR

N_{rev} = numbers of revolutions per second

The expected number of events λ_i in Δt_i, is a function of

- the nominal beam momentum, p_{lab}, and the beam profile Π (E), E is the CM energy of the system.
- the parameters of the resonance

  the partial width $\Gamma_{p\bar{p}} = Br\,(\chi_1 \rightarrow p\bar{p}) \times \Gamma$

  the full width Γ

  the χ_1 mass m_{χ_1}
- the detection efficiency ϵ

and can be written

$$\lambda_i = \mathscr{L}\,\epsilon \int dE\, \Pi_i\,(E)\, \sigma\,(E, m_{\chi_1}, \Gamma, \Gamma_{p\bar{p}})$$

where the cross section σ for resonant formation has the Breit – Wigner behaviour:

$$\sigma(E, m_{\chi_1}, \Gamma, \Gamma_{p\bar{p}}) = (2J + 1)/[(2S_p + 1)\,(2S_{\bar{p}} + 1)]\,\pi\,\lambdabar^2 \times$$

$$Br(\chi_1 \rightarrow J/\psi\,\gamma)\,Br(J/\psi \rightarrow e^+\,e^-)\,\Gamma\,\Gamma_{p\bar{p}}/\,[(E - m_{\chi_1})^2 + \Gamma^2/4]$$

where

E = is the CM energy of the system

S_p = 1/2 ,spin of the proton

$S_{\bar{p}}$ = 1/2 , spin of the antiproton

J = 1 , total angular momentum of the χ_1 state

$\lambdabar$ is the De Broglie wavelength of the initial state and is rewritten as:

$\lambdabar^2 = \hbar^2/p^2 = 4\,\hbar^2/(E^2 - 4\,m^2)$, $\hbar^2 = (0.19733 \text{ fm GeV/c})^2$

m = proton mass

From ref [6] we have:

$Br(\chi_1 \rightarrow J/\psi\ \gamma) = 0.28 \pm 0.03$

$Br(J/\psi \rightarrow e^+ e^-) = 0.074 \pm 0.012$

The beam profile $\Pi_i(E)$ may be described as the sum of two half Gaussians joining at the momentum value of the peak intensity p_{peak}. E is transformed as $E = \sqrt{2\,m(m + \sqrt{m^2 + p^2_{lab}})}$, giving

$$\Pi_i(p_{lab}, p_{peak}, \sigma_\pm) = 1/N_i \ \exp\{-1/2\,[p_{lab} - p_{peak}]^2/\sigma_\pm]\}$$

where N_i, the normalisation factor is:

$$N_i = \int_{\Delta E_i} \Pi_i(E)\, dE = \int_{\Delta p_{lab}} \Pi_i(p_{lab}) dE/dp_{lab}\, dp_{lab}$$

$\Delta\, p_{lab}$ is found from $\Delta\, E_i$ using $E = \sqrt{2\,m\,(m + \sqrt{m^2 + p^2_{lab}})}$ and we have:

$$dE/dp_{lab} = m\, p_{lab}/\{\sqrt{m^2 + p^2_{lab}}\, \sqrt{2\,m(m + \sqrt{m^2 + p^2_{lab}})}$$

giving

$$N_i = \int_{\Delta\, p_{lab}} m\, p_{lab}/\{\sqrt{m^2 + p^2_{lab}} \sqrt{2m(m + \sqrt{m^2 + p^2_{lab}})}\} \times$$
$$\exp(-1/2\{[p_{lab} - p_{peak}]/\sigma_\pm\}^2\ dp_{lab}$$

where σ_+ is used when $p_{lab} < p_{peak}$ and σ_- is used when $p_{lab} > p_{peak}$.

Given an expression for the number of events λ_i expected in the time interval Δt_i, the likelihood function can be written down as:

$$L = \prod_{i=1}^{k} P(n_i|\,\lambda_i) = \prod_{i=1}^{k} \lambda_i^{n_i}\, e^{-\lambda_i}/n_i!$$

k = number of time intervals Δt_i.

since it is known that if we expect λ_i events during Δt_i, the distribution of the observed number of events n_i follows the Poisson distribution.

$$P(n|\lambda) = \lambda^n\, e^{-\lambda}/n!$$

Instead of maximising L it is more convenient to minimise the equivalent expression $-\ln L$. This was done using the minimisation package MINUIT [44]. Several minimization procedures are offered by this package. The one most suitable for our applications was the variable metric (Fletcher) minimisation [45]. The results of this minimisation are given in the next section.

4.3 THE RESULTS

Using the information about the beam profile Π (E) and the luminosity $\mathscr{L}_i$ in the time intervals Δt_i, the likelihood function L was calculated and the expression $-\ln L$ minimised. Two different estimates were performed:

a. One in which the mass, the total width, the partial width for χ_1 to $p\bar{p}$ and the detection efficiency were the parameters.

b. One in which the mass, the total width, the branching ratio for $\chi_1 \to p\bar{p}$ and the detection efficiency were the parameters.

Below results from both estimates are given.

4.3.1 The χ_1 mass

The χ_1 mass was estimated to be:

$$m_{\chi_1} = (3511.3 \pm 0.2 \pm 0.4) \text{ MeV}$$

where the first error is statistical and the second error being the systematic error from beam momentum calibration. This result should be compared with the Crystal Ball result [13] $m_{\chi_1} = 3512.3 \pm 0.3 \pm 4.0$. Note the improvement of a factor 10 in the systematic errors. See also table 8 .

4.3.2 The total width Γ

Only an upper limit could be set on Γ, the momentum resolution in the experiment not being good enough to give the total width. Also due to lack in time due to the ISR close-down, less time had to be spent on each resonance. Given more time, maybe a precise value could have been given. It was found that

$$\Gamma < 1.3 \text{ MeV (at 95 \% Confidence Level)}$$

which indicates the narrowness of the χ_1 state. If we compare Γ_{χ_1} with Γ_{χ_2}, we see that

$$\Gamma_{\chi_2}/\Gamma_{\chi_1} > 2$$

which agrees with QCD in which this difference is explained by the not allowed 2g annihilation channel for the χ_1 state.

4.3.3 The branching ratio $Br(\chi_1 \rightarrow p\bar{p})$ *and the partial width* $\Gamma_{p\bar{p}}$

The partial width was estimated by method a.

$$\Gamma_{p\bar{p}} = (57 \pm 15) \text{ eV}$$

where ± 15 are the statistical errors.

The branching ratio was estimated by method b.

$$Br\,(\chi_1 \rightarrow p\bar{p}) > 0.6 \times 10^{-4} \quad (95\ \%\ \text{C. L.})$$

4.3.4 THE DETECTION EFFICIENCY

The detection efficiency ϵ was also included in the maximum likelihood estimate. This to get a better idea of detector performance and analysis efficiency. The efficiency ϵ_{est} can be estimated as follows:

$$\epsilon_{est} = \epsilon_c \times \epsilon_G \times \epsilon_A$$

where

ϵ_C is the Cerenkov efficiency. If it is assumed that the number of photoelectrons n, is Poisson distributed

$$P(n) = e^{-\nu}\, \nu^{n}/n!$$

Table 8: χ_1 and χ_2 parameters, Crystal Ball and R704.

	Crystal – Ball		R704	
State	m(MeV)	Γ(MeV)	m(MeV)	Γ(MeV)
χ_1	$3512.3\pm0.3\pm4.0$	< 3.8	$3511.3\pm0.2\pm0.4$	< 1.3
χ_2	$3557.8\pm0.2\pm4.0$	$(0.85-4.9)$	$3556.9\pm0.4\pm0.5$	2.6 ± 1.4

The first(second) error is statistical(systematic).

with a mean number of photoelectrons $\nu = <N_{pe}> = 5.5$, and that 1.5 photoelectrons are required by the trigger we get a Cerenkov efficiency for each arm:

$$\epsilon_{Ci} = 1 - P(1.5) = 0.97 \quad , \quad i = 1,2$$

which gives in total:

$$\epsilon_C = \epsilon_{C1}\epsilon_{C2} = 0.94$$

ϵ_G is the geometrical acceptance estimated by Monte Carlo calculations:

$$\epsilon_G = 0.112 = 11.2\ \%$$

ϵ_A is the analysis efficiency. For χ_1, $\epsilon_A \cong 97\ \%$ Finally we get:

$$\epsilon_{est} = 0.94 \times 0.11 \times 0.97 \cong 10\ \%$$

The detection efficiency ϵ found by the maximum likelihood estimate was:

$$\epsilon = (9.4 \pm 0.2)\ \%$$

well in agreement with the estimated one.

4.4 CONCLUSION

The R704 experiment performed at the CERN ISR studied charmonium spectroscopy using a new technique of $c\bar{c}$–formation in $p\bar{p}$– annihilation. In this work the χ_1 state has been studied. 31 χ_1

events were seen over a background of 0.7 events. The χ_1 mass, m_{χ_1}, the full width Γ and Br ($\chi_1 \to p\bar{p}$) were estimated by the maximum likelihood method. The following values were obtained:

m_{χ_1} = (3511.3 ±0.2 ± 0.4) MeV

Γ < 1.3 MeV (95 % C.L.)

$Br(\chi_1 \to p\bar{p}) > 0.6 \times 10^{-4}$ (95 % C. L.)

$\Gamma_{p\bar{p}}$ = (57± 15) eV

Thus in a small statistics experiment previous measurements of the χ_1 mass were confirmed, errors improved, the first measurement of the χ_1 partial width into $p\bar{p}$ obtained and a tighter bound set on the total width.

Appendix A

PROPORTIONAL CHAMBERS

The first multiwire proportional chamber was constructed and operated by Charpak and his collaborators in 1967 − 68 [47] and has since been used in most hig − energy physics experiments. Below a short description of how these chambers work are given. A more detailed description can be found in [48].

A fast charged particle traversing a gaseous or condensed medium has an average differential energy loss due to Coulomb interactions given by the Bethe − Bloch formula (not valid for electrons) :

$$dE/dx = -k\ Z/A\ \pi/\beta^2\ \{\ln[2\ m\ c^2\ \beta^2\ E_M/I(1-\beta^2)] - 2\beta^2\}\ ,$$

$$K = 2\pi\ N\ z^2\ e^4/m\ c^2$$

where N is the Avogadro number, z the charge and β the velocity (in units of c, the speed of light in vacuum) of the particle. m and e are the electron mass and charge, Z, A and ρ the atomic number and mass, and ρ the density of the medium. I is the ionization potential and E_M the maximum energy transfer allowed in each interaction between the particle and the medium.

$$E_M = 2\ m\ c^2\ \beta^2/(1-\beta^2)$$

The formula for dE/dx depends only on the particle velocity β, not its mass. Hence, after a fast decrease the energy loss reaches a minimum value for $\beta \cong 0.97$ and then slowly increases for $\beta \rightarrow 1$. The region of minimum loss is called the minimum ionizing region, see fig. 37 (also recall the expression minimum ionizing particle).

The energy loss distribution in thin media was first described by Landau:

$$f(\lambda) = 1/\sqrt{2\pi}\exp(-\ 1/2\,[\lambda + e^{-\lambda}])$$

where

$$\lambda = [\Delta\ E - (\Delta\ E)_{mp}]/\xi$$

$$\xi = K\ Z/A\ \rho/\beta^2\ x$$

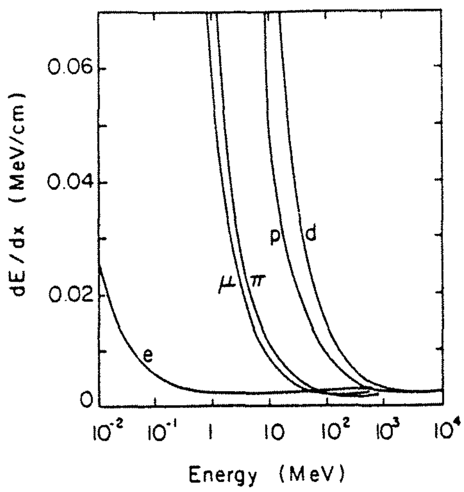

Figure 37: Energy loss per unit length in air computed by the Bethe – Bloch formula for different particles as a function of their energy. At energies above 1 GeV/c or so all particles loose about the same amount of energy (minimum ionization plateau). From [48].

λ represents the normalised deviation from the most probable energy loss $(\Delta E)_{mp}$ and x is the length traversed by the particle in the medium.

The energy loss of the particle is due to excitation and ionization of the constituent atoms in the medium. In the case of ionization the charged particle will liberate electron – ion pairs (primary ionization). The ejected electron may have an energy higher than the ionization potential of the medium and produce secondary electron – ion pairs (secondary ionization). The total ionization is the sum of of these two. The total number of electron – ion pairs n_T produced is:

$$n_T = \Delta E / W_i$$

where ΔE is the total energy loss in the medium and W_i the effective average energy necessary to produce one electron – ion pair. In a 1 cm thick (70 – 30) % mixture of argon – isobutane (recall the gas mixture in the MWPC's in R704) the total number of ion pairs produced by a particle is:

$$n_T = 2440/26 \cdot 0.7 + 4500/23 \cdot 0.3 = 124 \text{ pairs/cm}$$

The values of ΔE and W_i comes from [48] p. 2.

Hence a minimum ionizing particle traversing a mixture of argon (70 %) and isobutane (30 %) between the flat electrodes will give rise to a signal:

$$V = n_T\, e/C$$

where C is the capacitance of the system and e is the electron charge. Taking typical values $N_T \cong 120$ and $C \cong 10$ pF gives $V \cong 2\ \mu V$, a signal much to small to be detected. By introducing an much stronger electric field between the electrodes the signal size can be increased. The electrons liberated in the ionization process will gain energy in the field, avalanche multiplication occurs, see fig. 38, and the signal size can be improved by several orders of magnitude ($10^4 - 10^6$). The parallell plane detector has to be given up though due to severe limitations [48] and the coaxial cylindrical proportional counter is introduced, see fig 39.

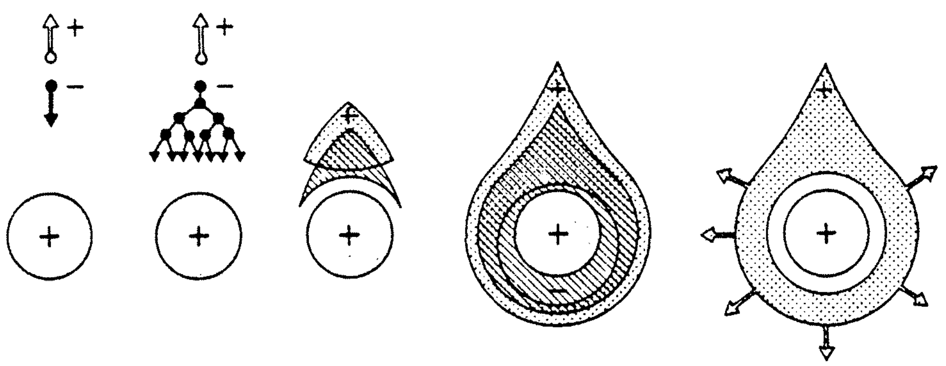

Figure 38: Time development of an avalanche in a proportional counter. A single primary electron proceeds towards the anode, in region of increasingly higher field, experiencing ionizing collisions; due to lateral diffusion, a drop-like avalanche develops. Electrons are collected in a very short time (~ 1 nsec) and a cloud of positive ions are left, slowly migrating towards the cathode.

The central wire, radius a, is kept at a positive potential with respect to the outer cylinder, radius b. The electric field is:

$$E(r) = C\, V_0/2\pi\varepsilon_0\ \ 1/r \quad , C = \pi\varepsilon_0/\ln(b/a)$$

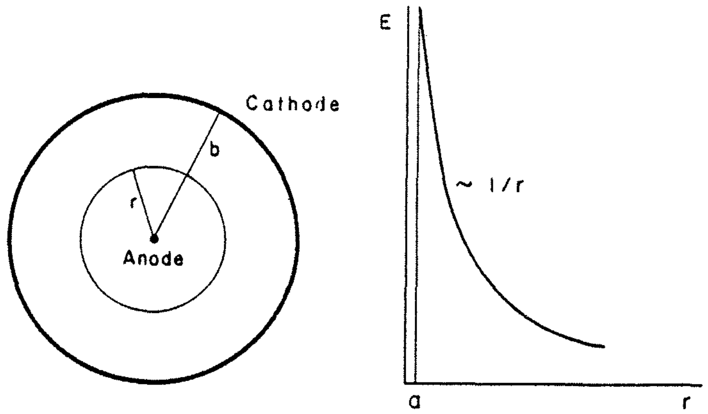

Figure 39: The coaxial cylindrical counter and the shape of the electric field around the thin anode. Only very close to the anode does the field grow strong enough to allow for avalanche multiplication. From [48].

and the potential

$$V(r) = C\, V_0/2\pi\varepsilon_0 \;\ln(r/a)$$

where ε_0 is the dielectric constant and $V_0 = V(b)$ is the overall potential difference, $V(a) = 0$.

The electric field is at maximum at the surface of the anode wire and the thinner the higher field and greater avalanche. The avalanche multiplication starts at a few wire radi (typical value for $a = 10\mu m$) when the field is strong enough. The main contribution to the signal does not come from the fast moving electrons, but from the much slower (~ 1000 times) ions. The induced signal by a charge Q moved a distance dr in a chamber is:

$$dQ = Q/V_0\; dV/dr\; dr = QC/2\pi\varepsilon_0\; 1/r\; dr$$

Assuming that all the charge MQ, M is the multiplication factor indicating the size of the avalanche multiplication, is produced at a distance λ from the wire we get:

$$q^- = -\,MQC/2\pi\varepsilon_0 \int_a^{a+\lambda} 1/r\,dr = -\,MQC/2\pi\varepsilon_0 \ln[(a+\lambda)/a]$$

$$q^+ = MQC/2\pi\varepsilon_0 \int_{a+\lambda}^{b} 1/r\,dr = MQC/2\pi\varepsilon_0 \ln[b/(a+\lambda)]$$

inserting typical parameters a = 10 μm, $\lambda \sim 1$ μm and b = 10 mm and taking the ratio:

$$q^-/q^+ \sim 10^{-2}$$

we clearly see that most of the signal is produced by the motion of the positive ions.

A multiwire proportional chamber consists of a set of thin, parallell and equally spaced anode wires, symmetrically sandwiched between two cathode planes, fig 40. Applying a negative potential to the

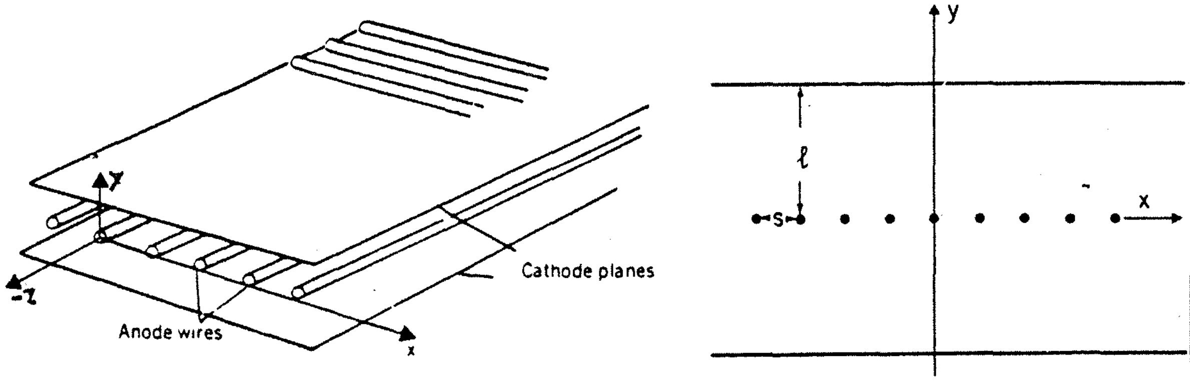

Figure 40: Layout of a multiwire proportional chamber. From [50].

cathode wires and grounding the anode wires an electric field as given in fig. 41 and fig. 42 develops. The electric field for $y \ll s$ is given by

$$E(x,y) \cong CV_0/2\pi\varepsilon_0\ 1/r\ ,\ r = \sqrt{x^2 + y^2}$$

showing that the field is radial around the anode wires as in the cylindrical proportional counter.

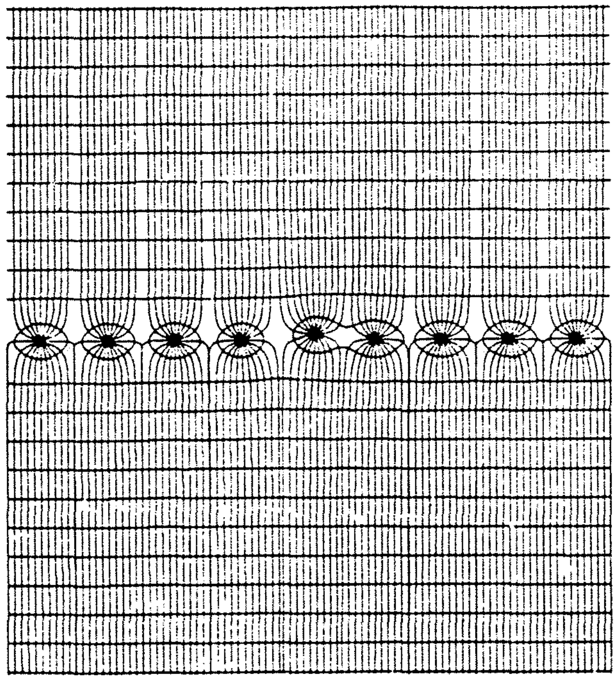

Figure 41: Electric field equipotentials and field lines in a MWPC. The effect on the field of a small displacement of one wire is also shown. From [48].

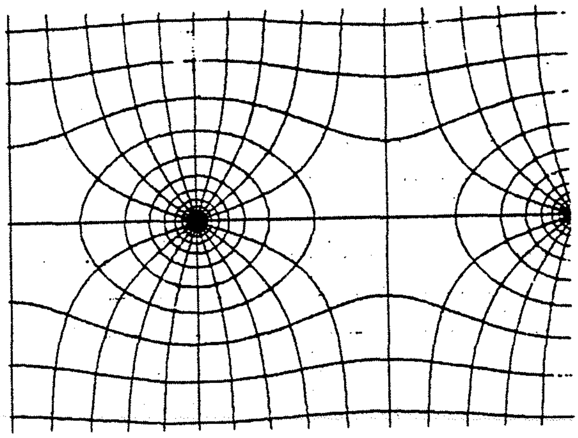

Figure 42: Enlarged view of the field around the anode wire. From [48].

It is normal to read out the signal from the anode wires. Combining information from several chambers with anode wires at different angles (e.g. MWPC, R704), may give resolution of $\sigma_x = \sigma_y = 0.6$ mm for a 2 mm wire pitch (R704, [29]). But also the the pulses induced on the cathodes can be read out [49]. By making the cathodes of strips orthogonal and parallell to the anode wires, see fig 17, and reading out the integrated pulse induced, a good resolution can be obtained : $\sigma_x = \sigma_y = 2.5$ mm (electrons) for a 10 mm pitch on cathode strips, analog chambers R704.

Appendix B

KINEMATICS OF THE PROCESS $\chi_1 \rightarrow J/\psi\, \gamma \rightarrow e^+ e^- \gamma$.

The directions of the electrons, $\vec{e}_i$ and $\vec{e}_j$, are known. Under the assumption of relativistic electrons ($m_e = 0$) , the electron momenta, photon direction and momentum are calculated. The proton mass, m_p, the antiproton mass, $m_{\bar{p}}$, the J/ψ mass, $m_{J/\psi}$ and the χ_1 mass m_{χ_1}, are all assumed to be known. We start with the 5 equations :

$$\vec{p}_{\bar{p}} = \vec{p}_i + \vec{p}_j + \vec{p}_\gamma \qquad (\vec{p}_p \cong 0 \text{ in the lab. system})$$

$$E_{lab} = E_i + E_j + E_\gamma$$

$$m_{J/\psi}^2 = (E_i + E_j)^2 - (\vec{p}_i + \vec{p}_j)^2$$

where :

$$E_{lab} = (m_{\chi_1}^2 - m_p^2 - m_{\bar{p}}^2)/\, 2m_{\bar{p}} + m_p$$

$p_{\bar{p}}$ being the momentum of the antiproton beam in the lab – system.

Also define

$$\gamma = E_{lab}/E_{CM}$$

We have thus a total of five equations and five unknowns. Using $\vec{p}_{\bar{p}} = 0 \cdot \vec{e}_x + 0 \cdot \vec{e}_y + p_{\bar{p}} \cdot \vec{e}_z$ we get on component form:

$$p_{i1} + p_{j1} + p_{\gamma 1} = 0$$

$$p_{i2} + p_{j2} + p_{\gamma 2} = 0$$

$$p_{i3} + p_{j3} + p_{\gamma 3} = p_{\bar{p}}$$

$$E_{lab} = E_i + E_j + E_\gamma$$

$$(m_{J/\psi})^2 = (E_i + E_j)^2 - \{(E_i)^2 + (E_j)^2 + 2\,\mathrm{dot})\} = 2\,E_i\,E_j\,(1-\mathrm{dot})$$

where

$$\mathrm{dot} = (p_{i1}\,p_{j1} + p_{i2}\,p_{j2} + p_{i3}\,p_{j3})/\,(E_i\,E_j) = \vec{e_i}\cdot\vec{e_j}\,,\ \vec{e_i} = \vec{p_i}/|\vec{p_i}|$$

The five unknowns being E_i, E_j and $\vec{p_\gamma}$ ($E_\gamma = |\vec{p_\gamma}|$) . Eliminating $\vec{p_\gamma}$ gives:

$$p_{\gamma 1} = -\,(p_{i1} + p_{j1}) \Rightarrow p_{\gamma 1}{}^2 = p_{i1}{}^2 + p_{j1}{}^2 + 2\,p_{i1}\,p_{j1}$$

$$p_{\gamma 2} = -\,(p_{i2} + p_{j2}) \Rightarrow p_{\gamma 2}{}^2 = p_{i2}{}^2 + p_{j2}{}^2 + 2\,p_{i2}\,p_{j2}$$

$$p_{\gamma 3} = -\,(p_{i3} + p_{j3}) + p_{\bar{p}} \Rightarrow p_{\gamma 3}{}^2 = p_{i3}{}^2 + p_{j3}{}^2 + 2p_{i3}p_{j3} - 2\,p_{i3}\,p_{\bar{p}} - 2\,p_{j3}\,p_{\bar{p}} + p_{\bar{p}}{}^2$$

$$E_{lab} = E_i + E_j + \sqrt{E_i^2 + E_j^2 + 2\,E_i\,E_j\,\mathrm{dot} - 2\,(p_{i3} + p_{j3})\,p_{\bar{p}} + p_{\bar{p}}{}^2}$$

$$m_{J/\psi}{}^2 = 2\,E_i\,E_j\,(1 - \mathrm{dot})$$

Eliminating E_i

$$E_i = m_{J/\psi}{}^2/\{2\,E_j\,(1 - \mathrm{dot})\} = C_4/E_j$$

gives:

$$E_{lab} = C_4/E_j + E_j + \sqrt{C_4{}^2/E_j{}^2 + E_j{}^2 + 2\,C_4\,\mathrm{dot} - 2\,(p_{i3} + p_{j3})\,p_{\bar{p}} + p_{\bar{p}}{}^2}$$

$$E_{lab}{}^2 - 2\,C_4\,E_{lab}/E_j - 2\,E_{lab}\,E_j + 2\,C_4 - 2C_4\,\mathrm{dot} + 2(p_{i3} + p_{j3})p_{\bar{p}} - p_{\bar{p}}{}^2 = 0$$

Setting $2\,C'_3 = E_{lab}{}^2 + m_{J/\psi}{}^2$, and remember $2\,C_4\,(1 - \mathrm{dot}) = m_{J/\psi}{}^2$

$$2\,C'_3 - 2\,E_{lab}\,E_j - 2\,C_4\,E_{lab}/E_j + 2\,(p_{i3} + p_{j3})\,p_{\bar{p}} - p_{\bar{p}}{}^2 = 0$$

$$p_{i3} = E_i\,p_{i3}/|\vec{p_i}| = E_i\,e_{i3}$$

$$2\,C'_3 - 2\,C_4\,E_{lab}/E_j + 2\,E_j\,e_{j3}\,p_{\bar{p}} - 2\,E_{lab}\,E_j + 2\,C_4\,e_{i3}\,p_{\bar{p}}/E_j - p_{\bar{p}}{}^2 = 0$$

$$2\,C'_3 - 2\,(E_{lab} - e_{i3}\,p_{\bar{p}})\,C_4/E_j - 2\,E_j\,(E_{lab} - e_{j3}\,p_{\bar{p}}) - p_{\bar{p}}{}^2 = 0$$

setting:

$$C_1 = E_{lab} - e_{i3}\, p_{\bar{p}}$$

$$C_2 = E_{lab} - e_{j3}\, p_{\bar{p}}$$

we get:

$$C_3' - C_1\, C_4/E_j - C_2\, E_j - 1/2\, p_{\bar{p}}^{\,2} = 0$$

where $p_{\bar{p}}^{\,2} = \beta^2\, E_{lab}^{\,2}$

now:

$$C_3' - 1/2\, p_{\bar{p}}^{\,2} = 1/2\,(E_{lab}^{\,2} + m_{J/\psi}^{\,2} - \beta^2\, E_{lab}^{\,2})$$

$$= 1/2\,[E_{lab}^{\,2}\,(1 - \beta^2) + m_{J/\psi}^{\,2}]$$

$$= 1/2\,(E_{CM}^{\,2} + m_{J/\psi}^{\,2}) = 1/2\, C_3$$

finally giving:

$$E_j^2\, C_2 - E_j\, C_3 + C_1\, C_4 = 0$$

where the unknown E_j is

$$E_j = (C_3 \pm \sqrt{C_3^2 - 4\, C_1\, C_2\, C_4}\,)/(2\, C_2)$$

giving:

$$E_i = (C_3 \pm \sqrt{C_3^2 - 4\, C_1\, C_2\, C_4}\,)/(2\, C_1)$$

and for the momentum of the photon:

$$p_{\gamma 1} = -\,(E_i\, e_{i1} + E_j\, e_{j1})$$

$$p_{\gamma 2} = -(E_i e_{i2} + E_j e_{j2})$$

$$p_{\gamma 3} = -(E_i e_{i3} + E_j e_{j3} - p_{\bar{p}})$$

$$E_\gamma = |\vec{p}_\gamma|$$

The uncertainties in the predictions were studied by Monte−Carlo calculations [40]. Sometimes the discriminant $C_3^2 - 4\,C_1\,C_2\,C_4 < 0$, due to measurements errors in the directions $\vec{e_i}$ and $\vec{e_j}$. The fraction of χ_1 events with negative discriminant was 7 $^0/_0$. In such cases the discriminant was set to zero in the calculations. The difference in angle (ω) between the generated and the reconstructed photon directions for all events and for those with negativ discriminant are given in fig. 43 .

Observe

all events	mean value $\approx 2^0$
neg. disc. events	mean value $\approx 7^0$

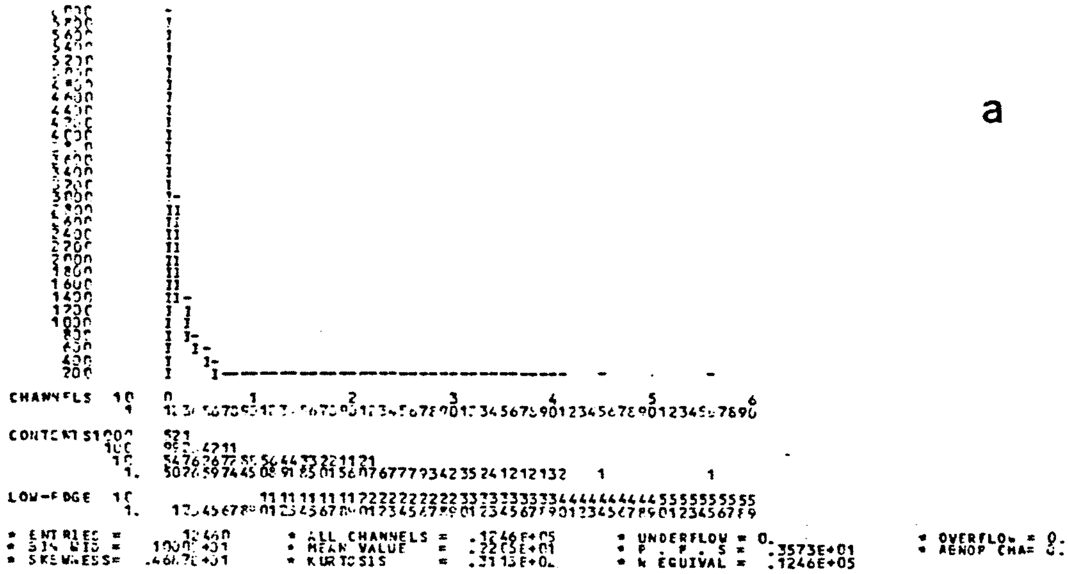

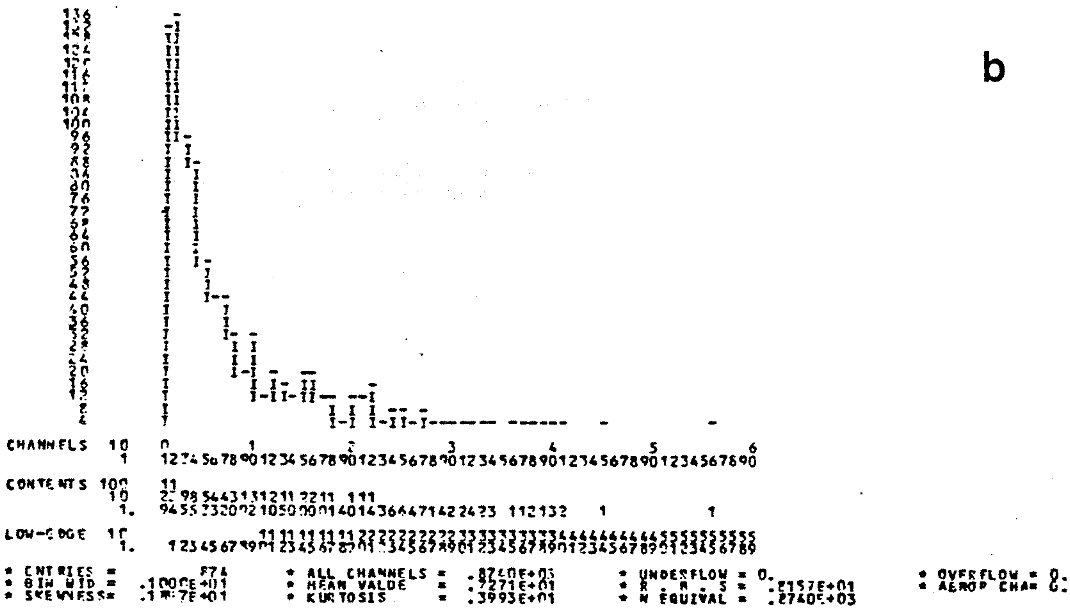

Figure 43: The uncertainty in the γ prediction from CHIDEC
a. All Monte Carlo generated events.
b. Events with negative discriminant.
From [40].

Appendix C

COORDINATE SYSTEMS IN R704

There were a total of three different coordinate systems, all with a common origo at the nominal vertex. The main system (x, y, z; right−handed) had the z−axis pointing in the beam direction. The two local systems in the arms (x′, y′, z′ and x″, y″, z″; both right−handed), were defined as shown below. Three reference planes z_r, z_r' and z_r'' were defined at a distance of 100 cm from the nominal vertex. The angle between a vector and the z−axis is the polar angle θ, while the azimuthal angle ϕ is the angle between the x−axis and the projection of a vector onto the xy−plane. The polar acceptance was $\theta \in [17°, 66°]$ and $\Delta \phi = 45°$, $\phi \in [-22.5°, 22.5°] \cup [157.5°, 202.5°]$.

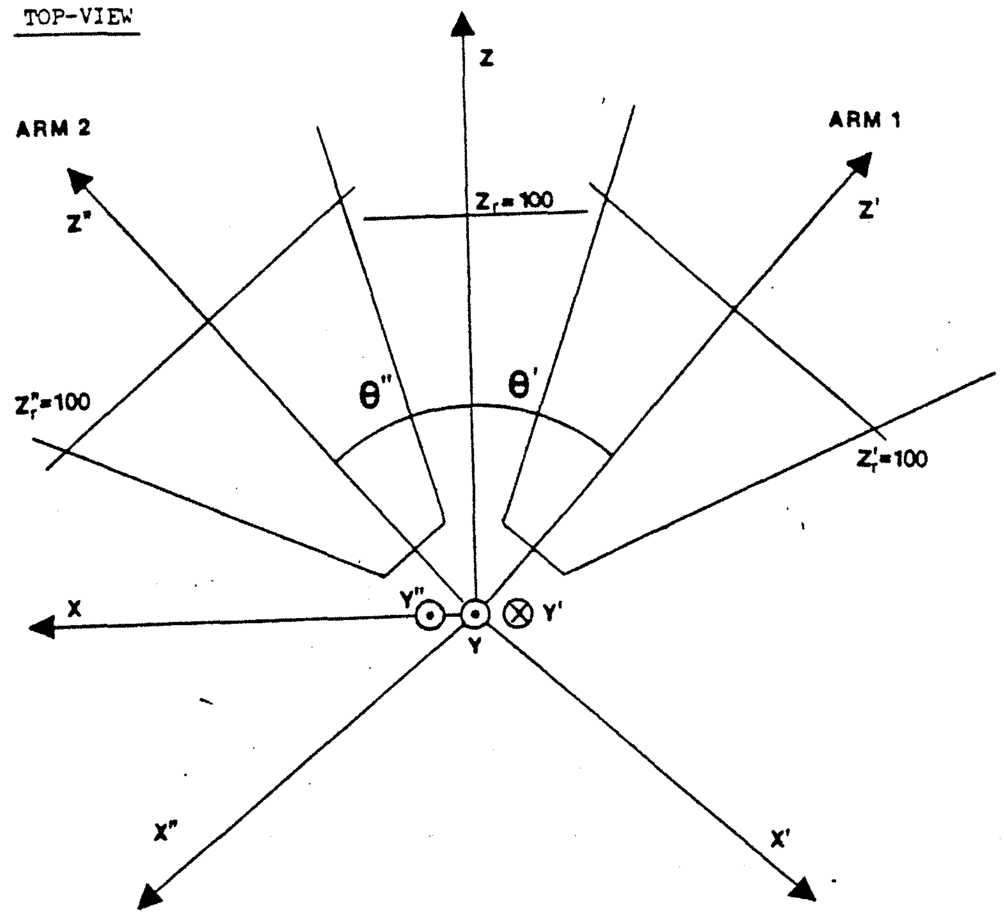

Figure 44: The different coordinate systems. From [31].

Appendix D

$^1P_1$ PRODUCTION AND ANALYSIS

A short description of the $^1P_1$ analysis together with the results from the Oslo group are given.

After filtering (energy – filter, see 3.2 filter b), 268 697 triggers were left for further analysis. Using the same production scheme as for for the χ_1 state (see 3.4), 2922 $^1P_1$ triggers passed the production stage. Of these 2922 triggers, 2 685 (92.4 %) passed the analog part and 613 (19.8 %) passed the digital part. More information about the production is given in table 9.

After the production cut a and b (see 3.5) were applied, a total of 1 360 $^1P_1$ triggers remained.

The rest of the analysis was done by B. Stugu and I will below briefly describe his final analysis together with the results obtained, see also [18].

Cut e was applied and the invariant mass of the electron pair required to be greater than 2.65 GeV. This left 236 triggers for further analysis.

The MWPC behaviour is believed to be well understood and only events having MWPC lines were accepted, reducing the number of triggers to 174.

Then the following cuts were applied:

a. Cut on the MWPC line quality:

- χ^2 of line[11] < 7
- vertexparameter < 2 cm

[11] The χ^2 of the line tells how good the fit of the MWPC clusters to the line is and is defined as:

$$\chi^2(\theta) = \Sigma\,(y_i - A_{ij}\,\hat{\theta}_j)^2$$

where the sum is over i, the clusters defining the line and $\hat{\theta}$ is the four line parameters x, y, dx/dz, dy/dz, y_i is the coordinate of plane i and A_{ij} is a constant matrix describing the dependence between the line parameters θ and the coordinates y. For a more detailed discussion see [31].

- absolute value of y and z vertex coordinates[12] < 1.3 cm

b.

a. Energy in precalorimeter arm 1 > 120 MeV

b. Energy in precalorimeter arm 2 > 160 MeV

c. C_1 and C_2 < 20 p.e.

d. Associated clusters to the lines in the MWPC should be closer than 3.2 cm in the precalorimeter and closer than 8.6 cm in the lead glass.

e. Reconstructed invariant mass > 2.65

---

[12] Track 1 and 2 in arm 1 and arm 2 can be described by:

track 1: $\vec{r}_1^{\,o} + s\,\vec{e}_1$

track 2: $\vec{r}_2^{\,o} + t\,\vec{e}_2$

where s and t are parameters. The crossing point of the two lines (vertex) can be found from the six equations:

$$\vec{r}_1^{\,o} + s\,\vec{e}_1 = \vec{r}_C$$

$$\vec{r}_2^{\,o} + t\,\vec{e}_2 = \vec{r}_C + 2\,d\,\vec{e}$$

where

$$\vec{e} = \vec{e}_1 \times \vec{e}_2 / |\vec{e}_1 \times \vec{e}_2|$$

is the direction of the shortest line crossing the two tracks and s, t, d and $\vec{r}_C$ are unknowns. The vertex defined to be on the middle of the shortest line crossing the two track is then:

$$\vec{r}_0 = \vec{r}_C + d\,\vec{e}$$

For a more detailed discussion see [31].

After applying these cuts 29 events were left for a visual scan. Of these 24 showed double peak structures in the precalorimeter or in the analog chambers. Thus a total of 5 inclusive ψ candidates were found and they are listed in table 10.

Table 10: The inclusive J/ψ's found in the $^1P_1$ search

Run	Event
1178	5688
1179	4718
1200	708
1230	1720
1248	10155

The efficiency of the $^1P_1$ analysis was estimated using the 187 J/ψ events.

a. MWPC reconstruction efficiency 175/187 = 93.6 %

b. Global efficiency 160/187 = 85.6 %

c. Efficiency of analysis when MWPC works 160/175 = 91.4 %

The efficiency is better estimated by analysing the χ_1 and the χ_2 events with $^1P_1$ chain. 25 of the 31 χ_1 events passed this analysis (80.6 %) while 45 out of the 59 χ_2 events were accepted (76.3 %), giving a global efficiency off 78 %.

The mass of the signal seen is:

$$m = (3525.8 \pm 0.5 \pm 0.5)\ \mathrm{MeV}$$

where the first (second) error is statistical (systematic). This result has to be compared with the c.o.g. of the spin avaraged ^3P_j states:

$$m(\mathrm{c.o.g.}) = \Sigma(2j+1)\, m_{\chi_J} / \Sigma(2J+1) = 3526\ \mathrm{MeV}$$

were the masses for χ_1 and χ_2 are taken from [52] and for χ_0 from [6]

The contribution of non−resonant inclusive J/ψ background to the 5 events is dominated by $p\bar{p} \rightarrow J/\psi\ \pi^0$, estimated to be of the order of 160 pb [51]. For an integrated luminosity L = 1193 nb^{-1}, a detection efficiency of 10 % and $Br(J/\psi \rightarrow e^+e^-) = 0.074$ about 1.4 background events should be present. 5 events were found with an integrated luminosity $L = 710\ nb^{-1}$, while in the χ_1 edges (of resonance) and $^1P_1$ edges zero events were found with an integrated luminosity $L = 483\ nb^{-1}$. However, the binominal probability for observing this configuration under a uniform background hypothesis is 7.5% , uncomfortable high.

The observed 5 events may be the first sign of the $^1P_1$ state of charmonium with a mass close to 3525 MeV. However, the statistics are marginal and future experiments are needed before a firm conclusion can be made.

Table 11: Analysis statistics for the $^1P_1$ search

Triggers started with ***	Cuts applied to the triggers	Triggers passing the analog part	Triggers passing the digital part	Triggers passing in total ***
***	Filtering	***	***	268 697
268 697	production	2 685	613	2 922
2 922	a	1 676	363	1 812
1 812	b	1 251	312	1 360
1 360	e + m−cut	***	***	236
236	MWPC lines	***	***	174
174	i − v	***	***	29
29	visual scan	***	***	5

Table 9: Production statistics for the $^1P_1$ search

RUN *** *** ***	Triggers started with ***	Triggers passing in total ***	Triggers passing analog part	Triggers passing digital part	CPU – time* *** *** ***
1161 – 1167	16992	188	178	41	8005.372
1168 – 1172	19336	185	171	39	8742.149
1174 – 1177	10527	111	97	33	4582.298
1178 – 1181	18942	218	202	53	9279.807
1182 – 1186	17362	188	178	32	8342.056
1187 – 1195	17606	171	156	30	8464.528
1196 – 1200	15318	160	150	29	7834.641
1201 – 1207	16790	187	173	42	7922.917
1210 – 1215	17727	168	153	35	8390.597
1216 – 1221	16985	175	163	27	7739.164
1222 – 1227	17459	198	186	35	8629.276
1230 – 1239	19576	249	224	63	9317.151
1240 – 1248	17599	192	179	35	8493.657
1249 – 1261	16372	204	186	40	7967.701
1262 – 1268	14427	172	146	47	6970.272
1269 – 1279	15679	156	43	52	7187.370
Toatally	268 697	2922	2685	613	121 850.316

* CPU seconds CDC CYBER

Appendix E

THE OSLO χ_1 EVENT SAMPLE

Table 12: The χ_1 events found in the Oslo analysis

RUN	EVENT
1090	8324
1097	2333
1097	9712
1098	5884
1101	9521
1103	18645
1104	3537
1104	8081
1107	11640
1109	5018
1111	13129
1111	13508
1113	23721
1117	13440
1139	10697
1140	1184
1142	10740
1143	12230
1144	15774
1148	14790
1148	15765
1149	17191
1150	3222
1150	8752
1151	2263
1152	221
1152	795
1154	290
1154	13431
1154	13906
1154	19690

REFERENCES

[1] J. J. Aubert et al., Phys. Rev. Lett. 33 (1974) 1404.

[2] J. E. Augustin et al., Phys Rev. Lett. 33 (1974) 1406.

[3] Y. Hara, Phys. Rev. B 134 (1964) 701.

[4] J. D. Bjorken and S. L. Glashow, Phys. Lett. 11 (1964) 255.

[5] S. L. Glashow, J. Illiopoulos and L. Maiani, Phys. Rev. D 2 (1970) 1285

[6] Particle properties. Data booklet, April 1984.

[7] E. Eichten, K. Gottfried, T. Kinoshita, K. D. Lane and T. M. Yan, Phys. Rev. D 17 (1978) 3090; 21 (1980) 203.

[8] J. L. Richardson, Phys. Lett. 82 B (1979) 272

[9] W. Buchmuller. Quarkonium Spectroscopy, from Fundamental Interactions in Low – Energy Systems. Edited by P. Dalpiaz, G. Fiorentini and G. Torelli (Plenum Publishing Corporation, 1985)

[10] A. Martin, Phys. Lett. 100B (1981) 511

[11] C. Quigg and J. L. Rosner, Phys. Lett. 71 B (1977) 153

[12] E.D.Bloom,Quark – Antiquark Bound State Spectroscopy and QCD, SLAC – PUB – 3015 November 1982 (T/E).

[13] J. Gaiser, Thesis, SLAC report 255 (1982).

[14] W. Buchmuller, Phys. Lett. 112 B (1982) 479

[15] For an introduction to the Thomas precession see e.g. E. Eriksen Classical Theoretical Physics II. Lecture notes University of Oslo (In norwegian)

[16] V. A. Novikov et al., Phys. Rep. 41 C (1978) 1

[17] G. Karl, S. Meshkov and J. Rosner, Phys Rev D 13 (1976) 1203

[18] Forthcoming Ph. D. thesis, Bjarne Stugu.(University of Oslo)

[19] F. E. Close, An introduction to Quarks an Partons, Academic Press 1979.

[20] Okubo. S. Phys. Lett 5 (1963) 165

Zweig, V. (1964 b) CERN Report No 8419/TH 912 (unpublished)

Iizuka, J. Prog Theor. Phys. Supplement (1966) No 37 – 38 p. 21.

[21] R. McClary and N. Byers, Phys. Rev. D28, (1983) 1692.

[22] P. Hasenfratz, R. R. Horgan, J. Kuti and J. M. Richard, Phys. Lett. 95 B (1980) 299.

[23] E. Eichten and F. Feinberg, Phys. Rev. D 23 (1981) 2724.

[24] D. Gromes, Z. Phys. C 22 (1984) 265.

[25] J. D. Jackson, Classical electrodynamics, 2nd Ed. (Wiley, New York, 1975).

[26] A. A. Zholentz et al., Phys. Lett. 96 B (1980) 214.

[27] E. D. Bloom and C. W. Peck, Ann. Rev. Nucl. Part. Sci. 33 (1983) 143.

[28] CERN/ISRC/80 – 14, ISRC/P106 29 April 1980. R704 proposal.

[29] C. Baglin et al. (R704 Collaboration), CERN EP Internal Report 85 – 01 18 January 1985.

[30] M. Macri , Gas Jet Targets, in Proceedings of CERN Accelerator School, Antiprotons for Colliding Beam Facilities, CERN, Geneva, Switzerland 11 – 21 October 1983, Ed. P. Bryant and S. Newman, CERN 84 – 15, 20 December 1984, p. 469.

[31] S. Stapnes, Thesis, University of Oslo (1985).

[32] C. Baglin et al. (R704 Collaboration), Contribution to the EPS International Europhysics Conference on High – Energy Physics, Bari (Italy) , 18/24 July 1985.

[33] J. B. Lindsay, C. Millerin, J. C. Tarle, H. Verwey and H. Wender A fast and flexible data acquisition system for multiwire proportional chambers and other detectors, Nucl. Instr. Methods, 156 (1978) 329.

[34] MICE, a fast user – microprogrammable emulator of the PDP – 11, CERN Data Handling Division DD/80/14 October 1980.

[35] J. P. Guillaud, R704 Internal note 100, On – line use of MICE for monitoring $p\bar{p} \rightarrow J/\psi$ and filtering $p\bar{p} \rightarrow \eta_c$ events in the R704 experiment.

[36] CAMAC, CERN DD Div. DD/OC/80 – 4 version 3 May 84

[37] E. Barrelet, R. Marbot, P. Matricon, A versatile microcomputer for high rate CAMAC data acquistion. Proceedings of the Topical Conference on the Application of Microprocessors to High Energy Physics Experiments at CERN, Geneva (1981) 258.

[38] Livingston, M. and Blewett, J. 1962 Particle Accelerators (McGraw – Hill)

[39] PATCHY FOR BEGINNERS, CERN DATA HANDLING DIVISION DD/EE/79−4, DD/US/60.

[40] D. Olsen, 13.02.85, R704 Internal note 124.

[41] PAM704D, the PAM−file on which the analysis program was stored.

[42] M. Chemarin, J. Fay, B. Mouellic, R704 Internal note 116.

[43] L. Bugge, A. Kylling, D. Olsen, B. Stugu, R704 Internal note 131.

[44] Function Minimization and Error Analysis, CERN long writeup D 506.

[45] R. Fletcher, Comput. J. 13 (1970) 317

[46] A. G. Frodesen, O. Skjeggestad and H. Tofte, Probability and Statistics in Particle Physics (Universitetsforlaget, Oslo, Norway, 1979).

[47] G. Charpak et el. Nuclear Instrum. Methods 62 (1968) 262.

[48] F. Sauli, Principles of operation of multiwire proportional and drift chambers. CERN Yellow Report 77−09.

[49] A. Breskin et al. Nuclear Instrum. Methods 143(1977) 29.

[50] K. Kleinknecht, Particle detectors, Phys. Rep. 84 (1982) 85.

[51] M. K. Gaillard, L. Maiani and R. Petroncio, Phys. Lett. 110 B (1982) 489.

[52] R704 collaboration, The formation of the χ_1 and the χ_2 states in $p\bar{p}$ annihilation, to be published.